



**Politecnico
di Torino**



Harvard John A. Paulson
School of Engineering
and Applied Sciences

Structured light with diffractive optics and metasurfaces

TESI DI LAUREA MAGISTRALE IN
NANOTECHNOLOGIES FOR ICTS

Author: **Alfonso Palmieri**

Student ID: s290291

Advisor: Prof. Carlo Ricciardi

Co-advisors: Ahmed Dorrah, Federico Capasso

Academic Year: 2022-23

Abstract

Diffractive optical elements (DOEs) such as spatial light modulators (SLMs), binary phase gratings, microelectromechanical systems (MEMS) and metasurfaces, have matured to the extent that they can reshape the scattered wavefront, i.e., altering the phase, amplitude and polarization of light. Metasurfaces — flat optic elements composed of subwavelength-spaced array of scatterers with spatially varying geometric parameters such as shape, size, orientation — are among the recent tools that can mould optical wavefronts into arbitrary shapes, point-by-point, with subwavelength resolution. Owing to the recent advances in nanofabrication, multi-layer metasurfaces have now become feasible. Here, we explore the possibilities offered by bilayer metasurfaces and show how it can overcome some of the intrinsic limitations of the widely adopted single layer metasurfaces. As an example, a new class of reflective bilayer metasurfaces is designed and fabricated. Such a device can, in principle, impart Pancharatnam-Berry phase on linearly polarized incident light as opposed to single layer Berry phase metasurfaces that primarily operate on circular polarization bases. In this process, we analyze the coupling within these bilayer structures and provide a design recipe for which this coupling can be neglected. In addition, we explore the use of programmable SLMs for generating new class of structured light beams; namely, optical vortices whose orbital angular momentum (OAM) can be adiabatically controlled along the optical path. We discuss the theoretical formalism, modeling, and experimental generation of this new class of beams and show that such an evolution in their OAM state is associated with a topological Berry phase factor that is accumulated along the propagation direction, at-will. Lastly, an outlook for this area of research and possible future directions are discussed.

Keywords: structured light, nanophotonics, metasurfaces, geometric phase, optical angular momentum.

Contents

Abstract	i
Contents	iii
1 Wavefront shaping with metasurface	1
1.1 Propagation of light	1
1.1.1 Jones calculus	2
1.2 Introduction to metasurfaces	3
1.3 Plasmonic metasurfaces	5
1.4 Dielectric metasurfaces	5
2 Building a single layer metasurface	9
2.1 Generate a library	9
2.2 Metasurface Polarization Optics	13
2.2.1 Dynamic and Geometric phase	13
2.3 The limitations of a single layer metasurface	15
3 The Bilayer Metasurface	19
3.1 The Jones matrix of a bilayer metasurface	19
3.2 The coupling between the layers	20
3.2.1 Bilayer simulations: the effect of the relative rotation	21
3.2.2 Bilayer simulation: bottom fin fixed and sweeping of the top fin	24
3.2.3 Bilayer simulations: sweep of the dimensions of both bottom and top nanofin: the fractal metasurface	28
3.3 The bilayer metasurface in reflection	30
3.3.1 Single layer metasurface in reflection	31
3.3.2 The addition of a silica spacer in a single layer metasurface working in reflection	34
3.3.3 Bilayer simulation: bottom fin fixed and sweeping of the top fin	37

3.4	A Pancharatnam–Berry phase-based bilayer metasurface	39
4	Dynamic wavefront shaping with SLMs	45
4.1	Principle and application of SLMs	45
4.2	Polarization-Transformations with Systems of Multiple SLMs	46
5	A new degree-of-freedom of light: Rotatum	49
5.1	Frozen waves	49
5.1.1	Mathematical formalism of Frozen waves	49
5.2	Orbital Angular Momentum	51
5.2.1	Superposition of OAM beams	53
5.3	Evolution of orbital angular momentum using frozen waves: step-like OAM transition	53
5.4	Continuous variation of topological charge along the propagation direction	56
5.4.1	Linear evolution of OAM	57
5.4.2	Parabolic evolution of OAM	59
5.4.3	Experimental measurements	60
5.5	Direct observation of spatially evolving Berry phase	63
6	Conclusions and future developments	69
	Bibliography	71
A	Appendix A - Bilayer simulation: the effect of a relative rotation of 45° sweeping the dimensions of the top nanofin fixing the dimension of the bottom nanofin	77
B	Phase retrieval algorithm	79
	List of Figures	81
	List of Tables	85
	List of Symbols	87
	Acknowledgements	89

1 | Wavefront shaping with metasurface

In the framework of metasurfaces, flat optic elements composed of subwavelength-spaced array of scatterers with spatially varying geometric parameters (such as shape, size, orientation), have been demonstrated to provide full control over the wavefront of incident light and its properties, including amplitude, phase and polarization[1]. In this section, we present a self-contained summary of polarization optics, introducing a mathematical treatment and language that is needed to represent polarization of light. Then, we review the history of metasurfaces, highlighting some of the optical properties of these devices for wavefront designs, focusing on the ability of these devices of controlling the polarization of light.

1.1. Propagation of light

Light is a portion of the electromagnetic spectrum, and its behavior is classically described by Maxwell's equations. Maxwell's equations can be combined, in a isotropic, nondispersive, and homogeneous medium, to yield the wave equation:

$$\nabla^2 \vec{E}(\vec{r}, t) = \mu\epsilon \frac{\partial^2}{\partial t^2} \vec{E}(\vec{r}, t) \quad (1.1)$$

where $\vec{E}(\vec{r}, t)$ is the electric field, \vec{r} represents the spatial coordinate and μ and ϵ are respectively the magnetic permeability and the electric permittivity of the medium. One of the possible solutions of Eq. (1.1) can be obtained by separation of space and time variables and it is represented by periodic functions of space and time known as "plane waves". In this case, the electric field is given by:

$$\vec{E}(\vec{r}, t) = \vec{E}_0(\vec{k} \cdot \vec{r} - \omega t) = \vec{E}_0 \text{Re}\{e^{i(\vec{k} \cdot \vec{r} - \omega t)}\} \quad (1.2)$$

where ω is the angular frequency and \vec{k} is the wave vector with $|\vec{k}| = \omega\sqrt{\mu\epsilon}$. At a given time t , Eq. (1.2) defines planes of constant phase given by \vec{r} with constant values of $\vec{k} \cdot \vec{r}$. In a uniform medium, substituting the expression of a plane wave into Maxwell's equations, it follows that $\vec{k} \cdot \vec{E}_0 = 0$ so the plane wave is a transverse wave that means that the electric field is confined to a plane perpendicular to its wave vector. In Cartesian coordinates, assuming $\vec{k} = k\hat{z}$, (without loss of generality) the plane wave's electric field is constrained to lie in the xy plane, and so it follows that:

$$\vec{E}(z, t) = (E_x e^{i\phi_x \hat{x}} + E_y e^{i\phi_y \hat{y}}) e^{i(\omega t - kz)} \quad (1.3)$$

that can be packaged in vector notation as:

$$\vec{E}(z, t) = \begin{pmatrix} E_x e^{i\phi_x} \\ E_y e^{i\phi_y} \end{pmatrix} e^{i(\omega t - kz)} \quad (1.4)$$

Rearranging the expression above, removing an overall phase and normalizing vector's amplitude it follows that:

$$\vec{E}(z, t) = E_0 e^{i\phi_x} \begin{pmatrix} \cos \chi \\ \sin \chi e^{i\phi} \end{pmatrix} e^{i(\omega t - kz)} \quad (1.5)$$

where $E_0^2 = E_x^2 + E_y^2$ and $\phi = \phi_y - \phi_x$. Equation (1.5) is very useful in order to describe the state of polarization of light.

1.1.1. Jones calculus

In order to describe the polarization of light, the propriety that specifies the geometrical orientation of the oscillations of the electric field, we review the basics of the Jones calculus: a matrix formalism to handle polarized light proposed by Robert Clark Jones[2–5]. From Eq. (1.5) it is possible to retrieve the "shape" of the electric field vector that is given by:

$$|j\rangle = \begin{pmatrix} \cos \chi \\ \sin \chi e^{i\phi} \end{pmatrix} \quad (1.6)$$

The expression reported in Eq. (1.6) is commonly referred to as a "Jones vector" and describes a shape that is in general an ellipse. Depending on the value of the parameters χ and ϕ we can distinguish between *linear*, *circular* and *elliptical* polarization. Cases

in which $\phi = 0$ describe oscillation of the electric field along a line, *linear* polarization. Cases in which $\chi = \pm\frac{\pi}{4}$ and $\phi = \pm\frac{\pi}{2}$ the ellipse traces out a circle (whose rotation is right-handed or left-handed) and in this case we talk about *circular* polarization. Other cases describe *elliptical* polarization. In order to describe how polarization state changes when light passes through optical elements, or perhaps after undergoing reflection or refraction at material interfaces, a 2x2 matrix known as Jones matrix \mathbf{J} . A Jones matrix, in the most general case, has 4 complex entries and maps one Jones vector $|j\rangle$ into another $|j'\rangle$:

$$|j'\rangle = \begin{bmatrix} J_{1,1} & J_{1,2} \\ J_{2,1} & J_{2,2} \end{bmatrix} |j\rangle \quad (1.7)$$

A given Jones matrix \mathbf{J} describe how a passive element can attenuate a given incident polarization, and it may advance or retard it in phase, or perform these operations selectively on orthogonal components of the polarization; the effect of a specific Jones matrix \mathbf{J} can perform a specific operation to a given Jones vector resulting in a given output that will be completely different from the output Jones vector when the same Jones matrix is operating on a different input, provided that linearity, and thus superposition, holds. A variety of optical devices have been proposed (and demonstrated), which enable modulation of polarization at optical frequencies; among them we are discussing in the next section about metasurfaces.

1.2. Introduction to metasurfaces

A metamaterial is defined as an artificial material whose physical properties are not found in nature. Among these it is worth citing negative refractive index ($n < 0$) able to focus and amplify evanescent waves, beating the traditional diffraction limit [6], or ϵ and μ values near 0[7]. Usually, metamaterials are made from assemblies of multiple elements, arranged in a repeating pattern and separated by sub-wavelength distances[8]. Metamaterials' physical properties rely mostly on their structures. Surface-type metamaterials are generally called metasurfaces. The word "metasurface" has a long history: the first time it has been used in literature was back in 1902, when Robert Wood found that the reflection spectra of subwavelength metallic grating had dark areas[9]. An explosion of metasurface research in optics can be traced to the publication of [10] in 2011 where, thanks to gold antennas with spatially varying phase response, an abrupt phase change over the scale of the wavelength is introduced at the interface between two materials. As a consequence of this patterning of the surface, anomalous reflection and refraction phe-

nomena are observed. The introduction of an abrupt phase shift, that is denoted in [10] as "phase discontinuity", at the interface between two media allows to revisit the laws of reflection or refraction applying Fermat's principle. Assuming to have an incident wave with an angle θ_i with respect to the normal to the interface between the two media and denoting with Φ and $\Phi + d\Phi$ the phase discontinuity, it can be proved (interpreting the phase gradient as an effective wavevector, leading to a generalization of the conservation of the wavevector parallel to the surface) that:

$$\sin(\theta_r) - \sin(\theta_i) = \frac{\lambda_0}{2\pi n_i} \frac{d\Phi}{dx} \quad (1.8)$$

$$\sin(\theta_t)n_t - \sin(\theta_i)n_i = \frac{\lambda_0}{2\pi} \frac{d\Phi}{dx} \quad (1.9)$$

where θ_r is the angle of reflection and θ_t is the angle of refraction. Equation (1.8) and (1.9) are respectively the generalized law of reflection and the generalized Snell's law of refraction that is obtained whenever a nonzero phase gradient is introduced at the interface between two media. These generalized laws indicate that the transmitted and reflected light beams can be bent into arbitrary directions in their respective half space, depending on the direction and magnitude of the inter-facial phase gradient, as well as the refractive indices of the surrounding optical media. In [10] the phase discontinuity is obtained patterning a silicon substrate with an array of plasmonic (gold) V-antennas leading to anomalously reflected and refracted beams in accordance with the generalized laws of reflection and refraction (Fig. 1.2).

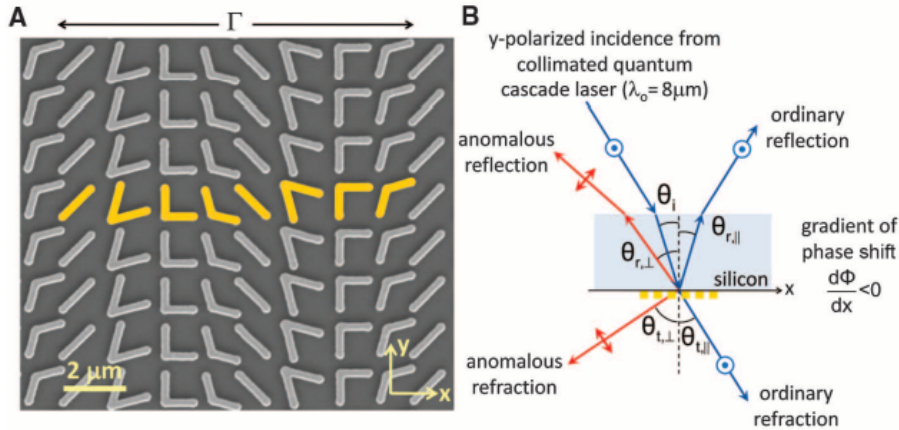


Figure 1.1: SEM image of gold V-antenna array on silicon and schematic experimental setup for y-polarized excitation (electric field normal to the plane of incidence). Figure from [10].

These arrays of gold antennas are the first example of what is now known as a "plasmonic metasurface".

1.3. Plasmonic metasurfaces

Earlier works on metasurfaces have utilized various metallic nanostructures with different shapes and orientations[11–13]: this class of metasurfaces is referred to as "plasmonic metasurfaces". In metallic nanostructures, resonant scattering of light by oscillating free electrons at the surface occurs due to a resonant electronic–electromagnetic oscillation known as localized plasmonic resonance (LPR). The rigorous treatment of time harmonic radiation of thin-wire antennas involves the solution of the electric field integral equation[14]. According to a simplified model, the LPR can be represented by a damped oscillator of a charge q with mass m driven by an incident electric field with frequency ω [15]. From second Newton's law it follows that:

$$\frac{d^2x}{dt^2} + \frac{\gamma}{m} \frac{dx}{dt} + \frac{k}{m}x = \frac{q}{m}E_0e^{i\omega t} + \frac{2q^2}{3mc^3} \frac{d^3x}{dt^3} \quad (1.10)$$

As it can be seen looking at Eq. (1.10), in addition to the ohmic losses (represented by the damping term γ and proportional to the velocity), another damping term (proportional to $\frac{d^3x}{dt^3}$) is needed to describe the recoil that the charge feels when it emits radiation. A possible solution of Eq. (1.10) is given by

$$x(t) = \frac{\frac{q}{m}}{(\omega_0^2 - \omega^2) + i(\omega \frac{\gamma}{m} + \omega^3 \frac{2q^2}{3mc^3})} \quad (1.11)$$

For $\omega \rightarrow 0$, from Eq. (1.11) it can be seen that the amplitude of oscillation is in phase with the incident field (so the phase delay is zero) while for $\omega \rightarrow \infty$ it is phase delayed by π . It follows that plasmonic metasurfaces using only resonant scattering do not achieve phase coverage of 2π so it is not possible to obtain full wavefront control. Furthermore plasmonic metasurfaces exhibit high optical losses at wavelengths shorter than the mid-IR not guaranteeing high scattering efficiency.

1.4. Dielectric metasurfaces

The highlighted limitations of plasmonic metasurfaces were overcome using dielectric resonators instead of metals, so introducing the so-called "dielectric metasurfaces": these metasurfaces are made of arrays of high-index dielectric light scattering particles whose

size is comparable to light’s wavelength[16]. The scattering proprieties of these particles were initially investigated by Faraday [17] and then deepened by Mie [18] whose analytical solutions of the fields are in accordance with the experimental data. Differently from plasmonic metasurfaces, dielectric metasurfaces provide controllable phase delay over the entire 2π range and at the same time almost unitary transmission efficiency. [19]. Initially amorphous silicon (an high-index dielectric with low loss) was used for applications in the telecom and near-IR spectral regions being also easy to manipulate since amorphous silicon structures can be fabricated depositing silicon as thin film on top of a substrate and then patterned with reactive ion etching (RIE) [16]. Then also other materials were used such as silicon nitride ([20]), single crystal silicon ([21]) and titanium dioxide ([22]) allowing to explore also the visible range. The individual structures comprising a dielectric metasurface can possess form birefringence; the latter is an effect that comes about when light interacts with anisotropically structured materials. The dimension of the individual scatterers, being comparable to the optical wavelength, allows to obtain birefringence also if the material involved is isotropic. Form birefringence specifically results when orthogonal polarization states experience different phase delays due to the shape of the fins of the dielectric metasurface: each individual element possesses two perpendicular axes of mirror symmetry if the shape is rectangular or elliptical. Light’s interaction with the fin is said to be similar to light propagation in a 2D waveguide with anisotropic cross section. From the symmetry of the rectangular or elliptical geometry, light linearly polarized along one axis or another will excite modes whose electric fields point along these directions as well. These modes experience different propagation constants, and accordingly different modal refractive indices, yielding form birefringence. The birefringence that is so obtained has been used to make up polarization-sensitive metasurfaces. Each individual structure, separated from its neighbors by less than a wavelength is commonly referred to as the metasurface’s “unit cell,” or the “meta-atom”. A metasurface is obtained stitching together these unit cells. Each meta-atom acts as a retarder imparting independent phase shifts on a basis of linear polarization states along the symmetry axes with an adjustable orientation. As a consequence the metasurface can be described by a Jones matrix that is spatially varying, enabling point by point polarization transformation:

$$\mathbf{J}(x, y)(\theta, \phi_x, \phi_y) = R(-\theta(x, y)) \cdot \begin{bmatrix} e^{i\phi_x(x, y)} & 0 \\ 0 & e^{i\phi_y(x, y)} \end{bmatrix} \cdot R(\theta(x, y)) \quad (1.12)$$

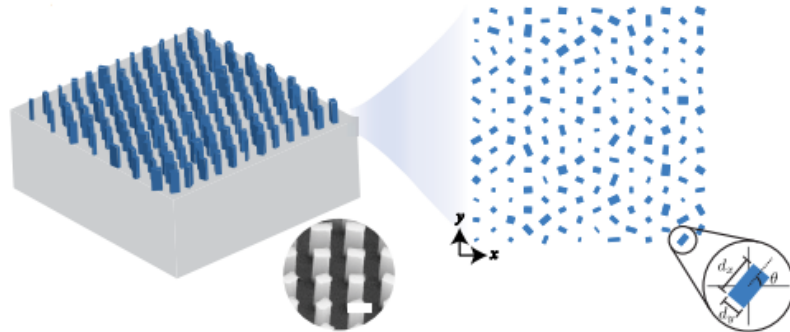


Figure 1.2: Model of dielectric metasurface. Figure from [23].

This almost unique propriety of metasurface combined with the intrinsic compactness of the device, have garnered significant interest in the last years, especially for polarimetry: metasurfaces were designed to obtain polarization beam splitters [24], polarization sensitive cameras [25], polarization insensitive lenses [26] and other innovative technologies that will unlock unprecedented possibilities.

2 | Building a single layer metasurface

In this section, we present a systematic strategy for designing a single layer metasurface. We start by building a metasurface library based on the results and ideas discussed in Ref. [27]. At the end of the section, we discuss the limits of single layer metasurfaces.

2.1. Generate a library

The first step was to replicate the results reported in [27]. To the aim of obtaining a direct relation between the phase shift and the dimension of the nanofins, a library has been generated by performing a parameter sweep with finite-difference time-domain (FDTD) simulations. In a simplified picture, each subwavelength structure can be considered as a truncated waveguide or a low-quality-factor Fabry-Perot resonator [28]. Nanofins with different dimensions (length and width) will induce different confinement of the field impinging on the structure. This confinement provides an effective refractive index that differs along the two polarization components. As it has been discussed in chapter 1, form birefringence is obtained thank to the subwavelength size of the fins so that, as exploited in the conventional waveplates, a different refractive index along orthogonal components is obtained. The FDTD software used is Lumerical: the software allows to solve Maxwell's equations on a discrete spatial and temporal grid in complex geometries such as the analyzed case.

A model of the simulated structure is the one shown in Fig. 2.1: it is formed by a fused silica substrate and a TiO_2 rectangular nanofin. The boundary conditions applied at the edges of the simulation box are the Periodic Boundary Conditions that emulate the existence of an infinitely periodic array of these rectangular fins so that the simulated structure is only the unit cell of the metasurface. The dimension of the basis, named D_x and D_y , ranged from 50 to 250 nm (for an overall of 2601 geometries) that is able to cover the range of phase from 0 to 2π and nearest-neighbor separation $d = 420$ nm that is the unit cell size. The structure is illuminated by an x-polarized plane wave source at 532 nm

that has been placed at a distance of 600 nm from the bottom basis of the substrate. At this wavelength the refractive index of the fused silica and of TiO_2 are set respectively to $0.811 + i0.366$ and 2.48. In order to compute the phase in the far-field and the percentage of transmitted power a monitor has been placed a few wavelengths above the top of the fin. The mesh size of this simulation is set to 10nm x 10nm x 10nm.

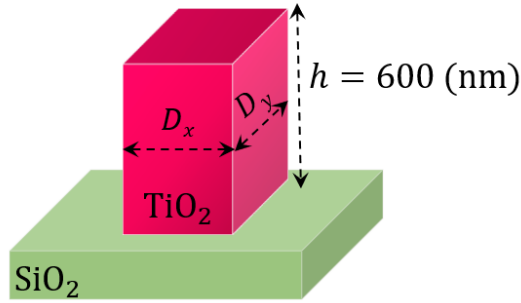


Figure 2.1: Unit cell of the single layer metasurface.

The obtained results are shown in Fig. 2.2 and they match the results obtained in [27]. It is necessary to note that the plots of the phase ϕ_y and of the power transmission T_y would be identical but with the x and y axes exchanged for the case of y-polarized source so they are not shown. As it was expected looking at the results shown in [27], the parameter space is able to completely cover the $0 - 2\pi$ range as it can be noticed from Fig. 2.2a. The Power Transmission plot (Fig. 2.2b) shows that the fins gives a almost uniform unitary transmission for fins with small D_x while some geometries with larger D_x manifests some resonances phenomena and a decrease in transmission. In the complex transmission plot shown in Fig. 2.2b the red dots correspond to the electric field amplitude $t_x e^{i\phi_x}$ of each simulated geometries. The average transmission is around 0.91 (black curve) and the red circle represent the unitary circle.

Thanks to the obtained results it is possible to map to each nanofin geometry a different Jones matrix.

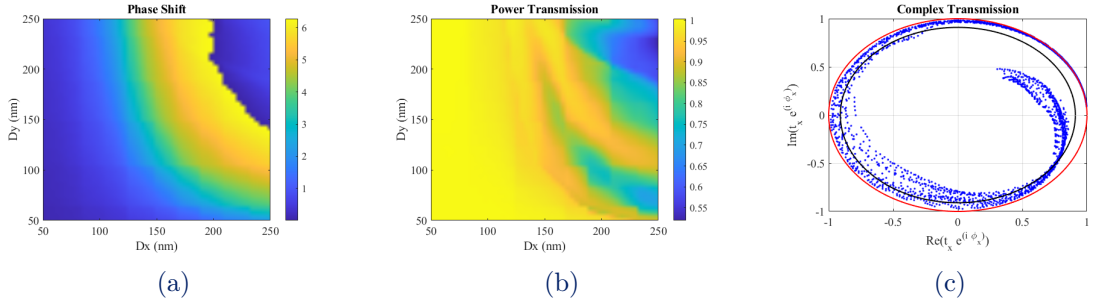


Figure 2.2: Simulation data for two-dimensional parameter sweeps of TiO_2 rectangular fins ($h = 600$ nm). **(a)** : Phase shift ϕ_x on x-polarized light. The phase shift has been computed as the ratio between the phase collected in the center of the far field projection of a monitor above the structure when the nanofin is present on top of the substrate and the phase at the same monitor when only the silica substrate is present. Units in radians. **(b)** : Power Transmission T_x for x-polarized light. The total power passing through a monitor above the structure relative to the source. **(c)** : Complex Transmission. The blue dots represent the electric field plotted on the complex plane for all the simulated geometries. The black circle corresponds to the averaged transmission. The red circle is the unit circle.

In the design of metasurface, it is possible to introduce a third degree of freedom: a rotation θ of the fin around its geometrical center as shown in Fig. 2.3. This is needed since the unitary symmetric Jones matrix associated to each simulated element would produce zero-valued elements in the anti-diagonal of each diffraction Jones matrix if no rotation angle is introduced.

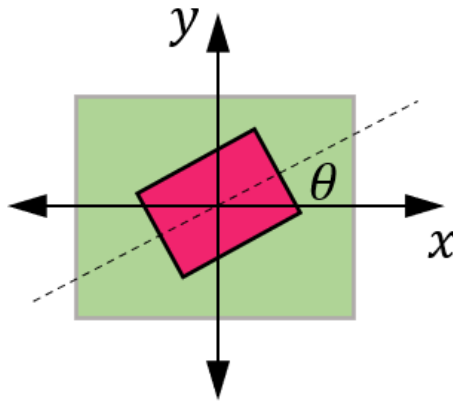


Figure 2.3: Unit cell of the single layer metasurface. The nanofin is rotated around its geometrical center by an angle θ .

The Jones matrix that describes a rotated nanofin can be modeled as follows:

$$\mathbf{J}(\theta, \phi_x, \phi_y) = R(-\theta) \cdot \begin{bmatrix} e^{i\phi_x} & 0 \\ 0 & e^{i\phi_y} \end{bmatrix} \cdot R(\theta) \quad (2.1)$$

where $R(\theta)$ is the 2×2 rotation matrix that is defined as:

$$\begin{bmatrix} \cos \theta & -\sin \theta \\ \sin \theta & \cos \theta \end{bmatrix} \quad (2.2)$$

The combination of the introduced rotation θ around the geometrical center of the nanofin and the linear structural birefringence enables the possibility to convert an incident vector state to another, locally, while achieving full 2π phase coverage as shown in Fig. 2.2a. From the obtained library it is so possible to pick, for example, a quarter wave plate (QWP) selecting the right geometry. The Jones matrix of a QWP is given by:

$$J_{QWP} = e^{\frac{i\pi}{4}} \begin{bmatrix} 1 & 0 \\ 0 & -i \end{bmatrix} \quad (2.3)$$

To select between the 2601 simulated geometries the ones acting as a QWP the following criteria were imposed:

- $|J_{11}| > 0.9$;
- $|J_{22}| > 0.9$;
- $|J_{22} - J_{11}| < 0.05$;
- $|\left| \angle J_{22} - \angle J_{11} \right| - \frac{\pi}{2}| < \frac{\pi}{36}$;

It turned out that there is more than one geometry able to satisfy the conditions listed above. Among them, we report in Table 2.1 the Jones matrix elements of two structure that satisfy the conditions listed above: the dimensions of the basis of the first structure (**QWP₁** in Table 2.1) are $134\text{nm} \times 202\text{nm}$ while the dimensions of the second structure (**QWP₂** in the Table 2.1) are $114\text{nm} \times 154\text{nm}$.

Jones matrix elements of selected QWP

	$ J_{11} $	$ J_{22} $	$ J_{11} - J_{22} $	$ \angle J_{22} - \angle J_{11} $
QWP_1	0.9636	0.9302	0.0334	86.58°
QWP_2	0.9775	0.9277	0.0498	89.9085°

Table 2.1: Jones matrix elements of two possible QWP

2.2. Metasurface Polarization Optics

Thanks to the created library it is possible to select the desired geometry for the design of the metasurface. The selection of the optimal geometry to impose a given phase can be performed by setting a threshold ϵ and saving the dimensions of all the geometries satisfy the following equation:

$$|t_{average}e^{i\phi_{desired}} - t_{simulation}e^{i\phi_{simulation}}| < \epsilon \quad (2.4)$$

At each point on the substrate, we place the optimum unit cell (420 nm in size) that is closest to the target phase shift required at that position. It is assumed that the light that is scattered by each nanofin is mainly affected by the geometrical parameters of the nanofin and has negligible dependence on the neighbouring nanofins so that each unit cell will act as a independent pixel. As a consequence, each nanofin will impose the desired polarization-dependent phase shift on the light that will be transmitted and modifies both the phase and the polarization of light. At this point it is necessary to highlight the difference between propagation phase design and geometrical phase design [28].

2.2.1. Dynamic and Geometric phase

By fixing the rotation angle θ of the nanofin around its geometrical center, while varying the nanofin dimensions it is possible to impose a phase shift ϕ_x and ϕ_y on any set of orthogonal, linear polarization using the so-called propagation (or dynamical) phase. As an example, using propagation phase design it is possible to build a device able to act as a different blazed gratings for orthogonal linear polarization states as described in [29]. Another relevant case is the chance to impart phase profiles of two independent phase holograms on orthogonal linear polarization states, yielding polarization-switchable far-

field holographic images [30, 31]. While propagation phase is so related to the variation of the optical path length (OPL), the geometric phase, is connected to polarization changes. The geometric phase is a phase factor acquired whenever a system undergoes a cyclic evolution governed by a slow change of parameters. Geometric phase is not strictly an optical phenomena neither a factor related to quantum mechanics [32]. The general concept of geometrical phase was introduced by sir. M. Berry [33]. From the adiabatic theorem, at any time t the system must be in an eigenstate of the Hamiltonian $H(\mathbf{R})$. Sir Berry showed that if the Hamiltonian's parameters slowly change, completing a full cycle, the final state of the system will be the same as the initial state with the addition of a phase factor called "geometric phase". This additional phase entirely depends on the geometry of the parameter's cyclic path. In optics, whenever light propagates through an anisotropic medium with a slowly varying change of its polarization, it acquires this geometric phase factor that is referred to as "Pancharatnam–Berry phase"[34]. In order to be able to recognize the geometric nature of the phase shift the key is to take advantage of the Poincaré sphere. The Poincaré sphere is a 2D mapping of the polarization vector space that allows to easily visualize polarization states on a unit sphere (Fig. 2.4).

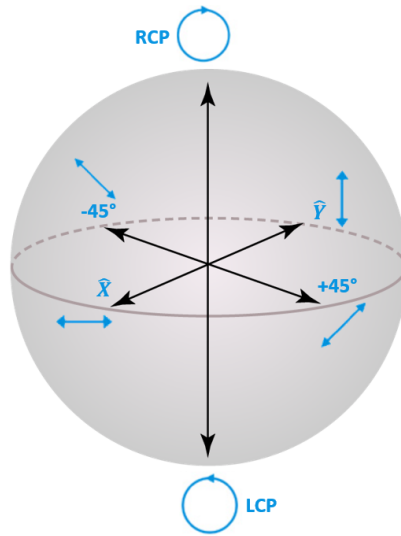


Figure 2.4: Poincaré sphere.

Linear polarization states conventionally lie on the equator of the sphere, the circular polarization (RCP and LCP) are located at the poles and the elliptical polarization states are located elsewhere. It is also possible to represent partially polarized light by locating them inside the sphere. Sir. Berry showed that a geometric phase is acquired if the polarization state traces a closed path on the Poincaré sphere. The acquired phase is exactly half the solid angle of the geodesic triangle spanned by the points on the Poincaré sphere.

The concept of Berry phase has been widely used in optics, also before the introduction of metasurfaces. In [35] a computer-generated subwavelength Pancharatnam–Berry phase-based diffraction grating is presented for imparting the desired phase at a wavelength of $10.6 \mu\text{m}$. The grating acts as a space-variant polarization state manipulator on a circularly polarized beam. The grating is designed so that the zero order has the same polarization as the impinging wave front and does not undergo any phase variation while the first diffracted order has acquired a phase factor that is purely geometrical so that it has change handedness.

2.3. The limitations of a single layer metasurface

As it has been highlighted in the first chapter, single layer metasurface have enabled the possibility to manipulate light in an unprecedented manner, finding application in holography, structured-light generation, and polarization control. On the other hand, the single layer suffers from some intrinsic limitations related to the restricted set of allowable Jones matrices. The Jones matrix of a single nanofin has to be a unitary symmetric Jones matrix in the linear polarization basis. The unitary of the Jones matrix is a consequence of the energy conservation in case a lossless medium is used (TiO_2 in our case) away from resonance. The symmetry of the Jones matrix can be proved using the reciprocity that links the original system to the case in which the propagation is reversed. The general 2x2 Jones matrix can be written as:

$$J = \begin{bmatrix} J_{1,1} & J_{1,2} \\ J_{2,1} & J_{2,2} \end{bmatrix} \quad (2.5)$$

and we suppose that this matrix is describing one nanofin of Fig. 2.5a. According to de Hoop reciprocity, the Jones matrix of the reciprocal system, where the structure remains the same and the propagation direction is reversed (Fig. 2.5b) can be written as:

$$J_{reciprocity} = \begin{bmatrix} J_{1,1} & -J_{2,1} \\ -J_{1,2} & J_{2,2} \end{bmatrix} \quad (2.6)$$

At the same time an inversion of the propagation direction can be obtained also with a mirror reflection with respect to the xy plane (Fig. 2.5c). The Jones matrix of the system can be obtained as:

$$J_{mirrored} = M \cdot J \cdot M^{-1} = \begin{bmatrix} J_{1,1} & -J_{1,2} \\ -J_{2,1} & J_{2,2} \end{bmatrix} \quad (2.7)$$

where M is the matrix describing the mirror given by $M = \begin{bmatrix} 1 & 0 \\ 0 & -1 \end{bmatrix}$. So comparing the expression of $J_{mirrored}$ and $J_{reciprocity}$ it follows that $B = C$ so the Jones matrix describing the nanofin of a single layer metasurface must be symmetric.

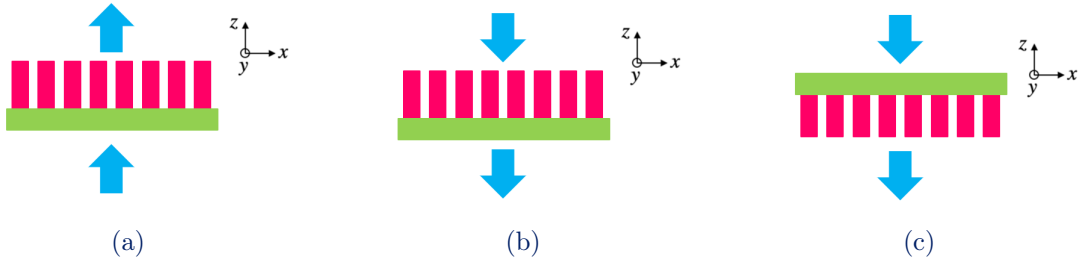


Figure 2.5: Symmetry analysis of a single layer metasurface **(a)** : Single layer metasurface, original situation, **(b)** : Reciprocal case: propagation direction is reversed. **(c)** : Mirrored system with reversed propagation direction.

It can be proved that if a Jones matrix is unitary and symmetric, then its eigenpolarization states are linearly polarized. If a Jones matrix is unitary it can be rewritten as

$$J = e^{i\phi} (e^{-i\frac{\alpha}{2}} \langle n|n \rangle + e^{i\frac{\alpha}{2}} \langle n_{\perp}|n_{\perp} \rangle) \quad (2.8)$$

where $\langle n|$ and $|n_{\perp}\rangle$ represent the eigenstates.

Being the Jones matrix symmetric, its transpose $J^T = J$. The expression of the transpose of J is:

$$J^T = e^{i\phi} (e^{-i\frac{\alpha}{2}} \langle n^*|n^* \rangle + e^{i\frac{\alpha}{2}} \langle n_{\perp}^*|n_{\perp}^* \rangle) \quad (2.9)$$

So comparing the expressions of J and J^T it follows that $|n^*\rangle = |n\rangle$ and $|n_{\perp}^*\rangle = |n_{\perp}\rangle$ so by definition these eigenstates are linear polarization states.

In principle these limits could be overcome using nanofins with tilted sidewalls with an angle that spatially varies but the fabrication process would be extremely complex in this case. As a consequence it is not possible to enable arbitrary conversion of amplitude,

phase and polarization with a single layer due to the constraints on the Jones matrix describing it. It is so necessary to introduce a new optical component able to embody any arbitrary passive Jones matrix array and gain complete control on coherent light transmission. In order to achieve this goal, in the next section, we explore the possibility offered by a bilayer metasurface that allows to overcome the limit of the symmetric Jones matrix.

3 | The Bilayer Metasurface

The concept of bilayer metasurface (Fig. 3.1) is a relative new one since the possibility of stacking multiple layers of metasurfaces has been limited by the complexity of the fabrication process in the last years [36–38]. In this section we list all the steps that were needed in order to design a bilayer metasurface. In order to obtain an optical component with a non-symmetric Jones matrix it is needed study the coupling between the two layers of the two layers of the proposed metasurface. We start by checking if the two layers can indeed be decoupled by considering metasurfaces in transmission and reflection modes. Intra-layer decoupling significantly simplifies the selection criteria when building a bilayer metasurface as it allows the user to run one FDTD simulation for the single layer library and reuse it to build the bilayer metasurface. Lastly, we proceed to report on a new class of Berry phase metasurfaces based on these bilayer structures.

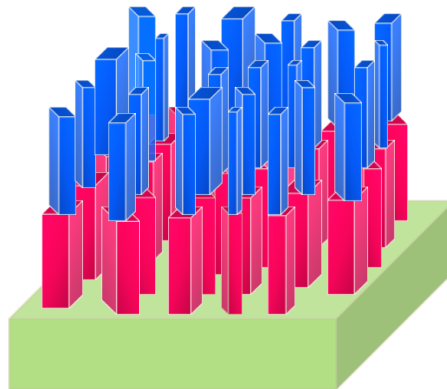


Figure 3.1: A schematic of the bilayer metasurface. It consists of two layers of TiO_2 rectangular nanofins fabricated on top of one another.

3.1. The Jones matrix of a bilayer metasurface

The addition of a second layer affords the possibility to access the entirety of retarder space (the entire sphere, with arbitrary overall phase control) so allowing the possibility of obtaining any possible Jones matrix thus relaxing the matrix symmetry constraint. It can

be proved that an arbitrary 2-by-2 unitary matrix can be decomposed into two unitary symmetric matrices, which is the key theoretical foundation at the basis of the design of a bilayer metasurface. The product of two arbitrary 2-by-2 unitary symmetric matrices each describing a single layer metasurface, can be written as:

$$\mathbf{J}_1 \cdot \mathbf{J}_2 = R(-\theta) \cdot \begin{bmatrix} e^{i\phi_x^1} & 0 \\ 0 & e^{i\phi_y^1} \end{bmatrix} \cdot R(\theta) \cdot R(-\theta') \cdot \begin{bmatrix} e^{i\phi_x^2} & 0 \\ 0 & e^{i\phi_y^2} \end{bmatrix} \cdot R(\theta') \quad (3.1)$$

where \mathbf{J}_1 and \mathbf{J}_2 are the Jones matrix of a single layer in the form Eq.(3.1), $R(\theta)$ is the 2×2 rotation matrix, θ and θ' are the rotation angle of the fins of the two layers, choosing $\phi_x^1 = 0$ and $\phi_y^1 = \pi$, Eq (3.1) be rearranged as follows:

$$\mathbf{J}_1 \cdot \mathbf{J}_2 = R(-2\theta) \cdot \begin{bmatrix} 1 & 0 \\ 0 & -1 \end{bmatrix} \cdot R(2\theta) \cdot R(-\theta') \cdot \begin{bmatrix} e^{i\phi_{x,2}} & 0 \\ 0 & e^{i\phi_{y,2}} \end{bmatrix} \cdot R(\theta') = \quad (3.2)$$

$$R(-\theta'') \cdot \begin{bmatrix} e^{i\phi_{x,2}} & 0 \\ 0 & e^{i\phi_{x,2}+\pi} \end{bmatrix} \cdot R(\theta') \quad (3.3)$$

where θ'' is defined as $\theta'' = 2\theta - \theta'$. For arbitrary $e^{i\phi_{x,2}}, e^{i\phi_{y,2}}, \theta$ and θ'' , the product $\mathbf{J}_1 \cdot \mathbf{J}_2$ expressed as in Eq. (3.3), according to [39], is a factorized form of an arbitrary 2x2 unitary matrix. This proves that the bilayer affords the possibility to access all possible unitary Jones matrix so that the constrain of symmetry of the single layer is overcome.

3.2. The coupling between the layers

In this section we explore the possibility to compute the Jones Matrix of the bilayer as the product of two Jones matrix of single layer metasurface. This implies that the coupling between the two fins is negligible and independent from the dimensions of the two fins and from a possible relative rotation between the two fins. In order to do so, we will compare the results of the FDTD simulations of the bilayer with the "analytical" results obtained starting from the data of the single layer reported in Fig. 2.2. We consider the bilayer unit cell reported in Fig. 3.2. The unit cell size is the same one of the single layer metasurface (420 nm). The two fins are made of TiO_2 have the same height (600 nm) and the dimension of the basis (D_x, D_y) of the nanofin can vary from 50 nm to 250 nm. We will refer to the two nanofins as "bottom nanofin" and "top nanofin". The rotation of the bottom nanofin will correspond to the parameter θ while the rotation of the top nanofin will correspond to the parameter θ' . Initially we will test the case of a bilayer metasurface

working in transmission mode: as it was for the single layer the structure is illuminated by a x-polarized plane wave source at 532 nm that has been placed at a distance of 600 nm from the bottom basis of the substrate (the vales of the refractive indices used are the same reported in the previous chapter). In order to compute the phase in the far-field and the percentage of transmitted power a monitor has been place a few wavelengths above the top of the nanofin. Also in this case, as it was for the single layer metasurface simulation, at the borders of the metasurface Periodic Boundary Conditions were applied while at the extremes of the simulation box along the z direction, PML were forced. Given the complexity of this structure and in order to obtain high accuracy, we used a fine mesh size of 2.5nm x 2.5nm x 2.5nm and we repeated the simulations of the single layer with this finer mesh to be consistent.

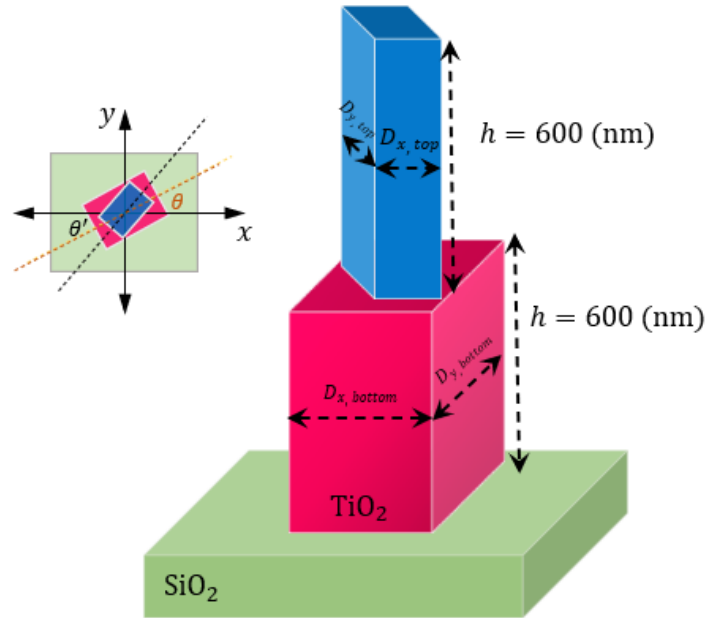


Figure 3.2: Unit cell of the bilayer metasurface.

3.2.1. Bilayer simulations: the effect of the relative rotation

The first case analyzed is the effect of a relative rotation between the two fins of the metasurface. Two cases are tested: in the first case we used the dimensions of the **QWP₁** (134nm x 202nm) both for the bottom and top nanofins while in the second case we used the dimensions of the **QWP₂** (114nm x 154nm). The rotation angle of the bottom nanofin is set to zero ($\theta = 0$) and we sweep the rotation of the top nanofin (θ') that can assume the values between 0 and 90 with a step of 15. The cases of rotation angle of the top nanofin $\theta' > 90$ can be analytically obtained from the analyzed ones from symmetry

argument. In Table 3.1 - 3.4 it is reported the element by element comparison between the Jones matrix of the simulated bilayer (\mathbf{J}_s) and the "analytical Jones matrix (\mathbf{J}_a)" obtained as follows:

$$\mathbf{J}_a = \mathbf{J}_{\text{top}} \cdot \mathbf{J}_{\text{bottom}} = R(-\theta') \cdot \begin{bmatrix} e^{i\phi_{x,\text{top}}} & 0 \\ 0 & e^{i\phi_{y,\text{top}}} \end{bmatrix} \cdot R(\theta') \cdot \begin{bmatrix} e^{i\phi_{x,\text{bottom}}} & 0 \\ 0 & e^{i\phi_{y,\text{bottom}}} \end{bmatrix} \quad (3.4)$$

where $R(\theta')$ is the 2×2 rotation matrix.

	$ J_{1,1;a} - J_{1,1;s} $	$ J_{1,2;a} - J_{1,2;s} $	$ J_{2,1;a} - J_{2,1;s} $	$ J_{2,2;a} - J_{2,2;s} $
$\theta' = 0$	0.0653	0	0	-0.0548
$\theta' = 15$	0.0307	-0.0154	0.0434	-0.0547
$\theta' = 30$	-0.0203	-0.0345	0.0148	-0.0386
$\theta' = 45$	-0.0281	-0.0404	-0.0280	-0.0155
$\theta' = 60$	-0.0398	-0.0381	-0.0443	-0.0101
$\theta' = 75$	-0.0643	-0.0257	-0.0328	-0.0225
$\theta' = 90$	-0.0776	0	0	-0.0323

Table 3.1: Element-by-element comparison between the magnitude of the Jones matrix elements of the simulated bilayer \mathbf{J}_s and the elements of the analytical Jones matrix \mathbf{J}_a for the QWP₁(134nm × 202nm)

	$\angle(J_{1,1;a}) - \angle(J_{1,1;s})$	$\angle(J_{1,2;a}) - \angle(J_{1,2;s})$	$\angle(J_{2,1;a}) - \angle(J_{2,1;s})$	$\angle(J_{2,2;a}) - \angle(J_{2,2;s})$
$\theta' = 0$	8.6°	0	0	2.5°
$\theta' = 15$	6.7°	6.5°	9.0°	3.5°
$\theta' = 30$	6.3°	6.6°	4.4°	3.5°
$\theta' = 45$	7.3°	7.0°	4.5°	3.9°
$\theta' = 60$	5.1°	6.5°	4.4°	-4.8°
$\theta' = 75$	4.4°	6.3°	4.2°	5.4°
$\theta' = 90$	3.2°	0	0	5.1°

Table 3.2: Element-by-element comparison of the phase of the Jones matrix elements of the simulated bilayer \mathbf{J}_s and the elements of the analytical Jones matrix \mathbf{J}_a QWP₁(134nm × 202nm)

	$ J_{1,1;a} - J_{1,1;s} $	$ J_{1,2;a} - J_{1,2;s} $	$ J_{2,1;a} - J_{2,1;s} $	$ J_{2,2;a} - J_{2,2;s} $
$\theta' = 0$	-0.0291	0	0	0.0112
$\theta' = 15$	-0.0343	0.0277	0.0122	0.0564
$\theta' = 30$	-0.0324	0.0174	-0.0036	0.0375
$\theta' = 45$	-0.0367	0.0029	0.0085	0.0025
$\theta' = 60$	-0.0523	-0.0002	-0.0005	-0.0309
$\theta' = 75$	-0.0609	0.0108	0.0158	-0.0469
$\theta' = 90$	-0.0560	0	0	-0.0439

Table 3.3: Element-by-element comparison of the magnitude of the Jones matrix elements of the simulated bilayer \mathbf{J}_s and the elements of the analytical Jones matrix \mathbf{J}_a for the QWP₂(114nm × 154nm)

	$\angle(J_{1,1;a}) - \angle(J_{1,1;s})$	$\angle(J_{1,2;a}) - \angle(J_{1,2;s})$	$\angle(J_{2,1;a}) - \angle(J_{2,1;s})$	$\angle(J_{2,2;a}) - \angle(J_{2,2;s})$
$\theta' = 0$	-1.8°	0	0	1.7°
$\theta' = 15$	-1.2°	-3.9°	1.6°	0.8°
$\theta' = 30$	-1.2°	1.7°	0.1°	1.2°
$\theta' = 45$	-1.6°	2.2°	0.7°	0.1°
$\theta' = 60$	-1.7°	0.2°	1.8°	1.3°
$\theta' = 75$	-2.6°	2.6°	3.4°	2.7°
$\theta' = 90$	2.2°	0	0	2.6°

Table 3.4: Element-by-element comparison of the phase of the Jones matrix elements of the simulated bilayer \mathbf{J}_s and the elements of the analytical Jones matrix \mathbf{J}_a QWP₂(114nm × 154nm)

The discrepancy that arises between the Jones matrix of the simulated bilayer and the "analytical Jones matrix" is on average not so large and can be considered acceptable for both cases both for phase and amplitude. This implies that, at least for the tested geometries, it is possible to use the formula reported in Eq. (3.4). In order to explain the errors it is necessary to remember that both in the simulation of the single layer metasurface and in the simulation of the bilayer metasurface, on the borders of the unit cell, Periodic Boundary Conditions were applied allowing to calculate the response of the entire system by only simulating one unit cell. When the simulation runs, the Periodic

Boundary Conditions simply copy the EM fields that occur at one side of the simulation and inject them at the other side. The results reported in Fig. 2.2 are so related to the case of no rotation of the fin: the Periodic Boundary Condition emulate the existence of an entire structure composed of all identical fins with zero rotation angle. The field obtained at the borders of the unit cell in the case of zero rotation angle will be so different from the case of a rotated fin. In the case of the simulated bilayer a rotation was superimposed on the top nanofin. As a consequence the results obtained starting from the library of a single layer and applying Eq. (3.4), being influenced by the PBC applied for the creation of the library, are different from the ones obtained in the simulation of the bilayer where a rotation of one the fins is present. From the data reported in the tables it can be also assumed that the discrepancy between the analytical and simulated case is higher in the case of the \mathbf{QWP}_1 maybe due to its bigger dimension with respect of \mathbf{QWP}_2 so a rotation of the fin of the case of the \mathbf{QWP}_1 will effect more the variation of the electric field.

3.2.2. Bilayer simulation: bottom fin fixed and sweeping of the top fin

Once it has been verified that the rotation of one of the two fins allows to use Eq. (3.4) to compute the Jones matrix of a bilayer metasurface at least for the tested structure, we moved to a much more computational intensive simulation (the simulation takes about 20 hours to be completed also due to the fine mesh used): we fixed the dimension of the bottom nanofin and we performed a parameter sweep for the dimensions of the top nanofin without introducing a rotation angle between the fins. This is needed since we want to verify if the two layers can be considered decoupled for all the geometries. If that's the case, then the Jones matrix of the bilayer can be expressed as:

$$\mathbf{J}_{\text{bilayer}} = \mathbf{J}_{\text{top}} \cdot \mathbf{J}_{\text{bottom}} = \begin{bmatrix} e^{i\phi_{x,1}} & 0 \\ 0 & e^{i\phi_{y,1}} \end{bmatrix} \cdot \begin{bmatrix} e^{i\phi_{x,2}} & 0 \\ 0 & e^{i\phi_{y,2}} \end{bmatrix} \quad (3.5)$$

As it was for the previous section we compared the results obtained from the simulation of the bilayer with the "analytical" ones that are obtained starting from the simulation of the single layer. The dimension of the bottom nanofin are the one of the \mathbf{QWP}_1 : 134nm x 202nm. As a consequence, for the bottom nanofin we used the Jones matrix of this element reported in Table 2.1: these value will be the same for all the bilayer, independently from the dimensions of the top nanofin. The results of the simulation are shown in Fig. 3.3.

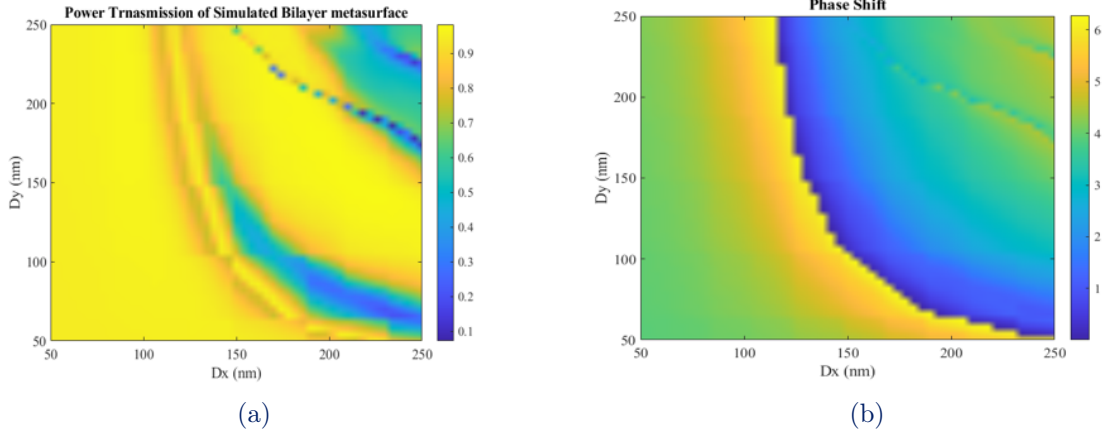


Figure 3.3: Simulation results of a bilayer metasurface with the dimension of the bottom fin fixed and are $134nm \times 202nm$: **(a)** : Phase shift ϕ_x on x-polarized light for a bilayer metasurface. Units in radians. **(b)** : Power Transmission T_x for x-polarized light. The total power passing through a monitor above the structure relative to the source.

The difference between the analytical Jones matrix and the simulated case are graphically visualized and shown in Fig. 3.4 and in Fig. 3.5. Each point of the plots represents the difference between the simulated and the analytical case for a different dimension of the top nanofin. From the plots it can be seen that Eq. (3.5) can be used for a wide range of geometries where the error is close to zero for both magnitude and phase for both J_{11} and J_{22} . The few geometries that exhibits a large error are the same ones that correspond to the resonance lines in the top right of the Fig. 3.3. This implies that for these geometries it is needed to simulate the whole structure while for all the other cases the library of a single layer to obtain the Jones matrix of the bilayer. In order to understand what happens at of the geometries for which the product of the Jones matrices of a single layer does not accurately reproduce the results of the simulation of the bilayer, a near-field analysis needs to be performed taking advantage of a different formalism such as the one of scattering matrices. From the simulation performed is also possible to confirm that the bilayer is able to cover the 0 to 2π phase range that is a necessary requirement for the design of a metasurface. This is shown in Fig. 3.6 looking at the z -axis: it can be noticed that the the 0 to 2π phase range is covered by the structure with low phase error with respect to the analytical case (represented by the color-map) so that it is possible to exclude the geometries that exhibit a large error.

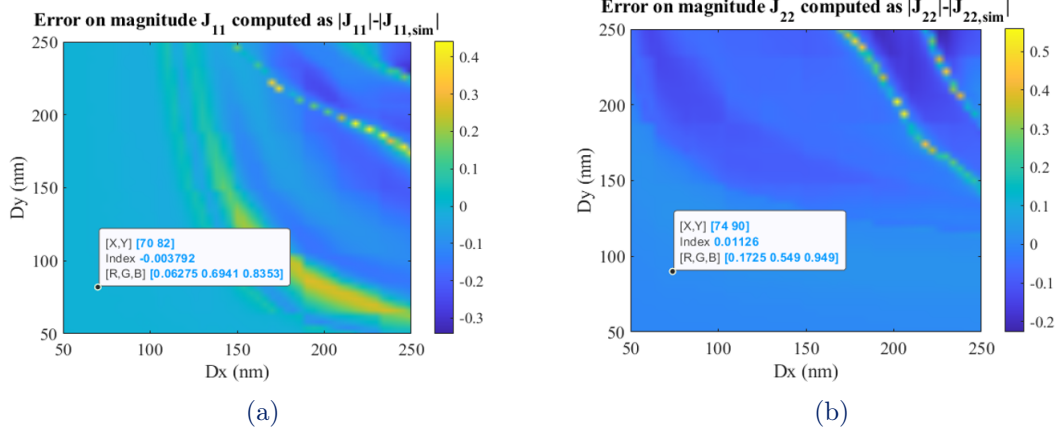


Figure 3.4: Plots of the difference in magnitude between the Jones matrix elements of the simulated bilayer with bottom fin fixed and the Jones matrix elements of a bilayer analytically computed: (a) : Difference between the phase of J_{11} extracted from the simulation and the phase of J_{11} analytically computed from the data of the single layer. (b) : Difference between the phase of J_{22} extracted from the simulation and the phase of J_{22} analytically computed from the data of the single layer.

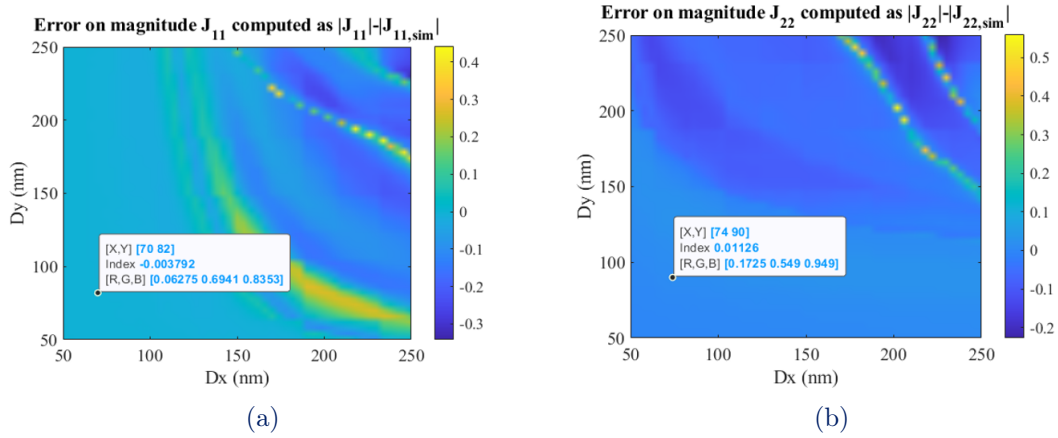
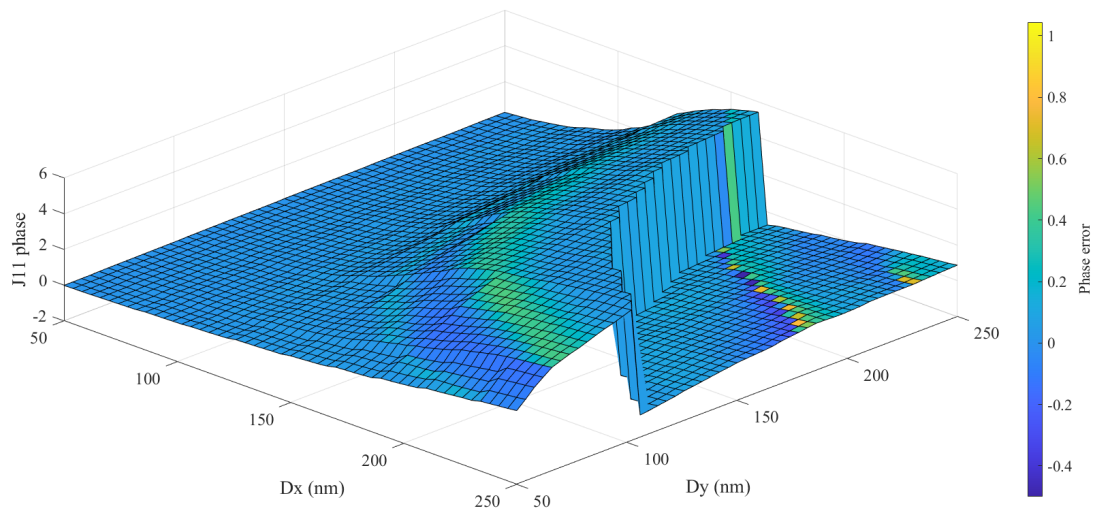
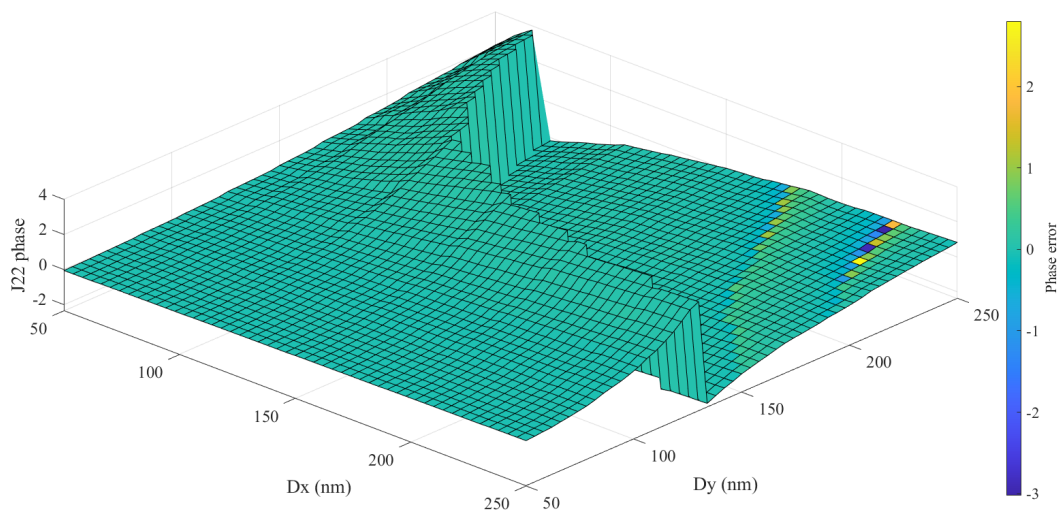


Figure 3.5: Plots of the difference in magnitude between the Jones matrix elements of the simulated bilayer with bottom fin fixed and the Jones matrix elements of a bilayer analytically computed: (a) : Difference between the magnitude of J_{11} extracted from the simulation and the magnitude of J_{11} analytically computed from the data of the single layer. (b) : Difference between the magnitude of J_{22} extracted from the simulation and the magnitude of J_{22} analytically computed from the data of the single layer.



(a)



(b)

Figure 3.6: Plots of the difference in phase between the Jones matrix elements of the simulated bilayer with bottom fin fixed and the Jones matrix elements of a bilayer analytically computed showing the ability of the bilayer metasurface to cover 0 to 2π phase range: **(a)** : Difference between the magnitude of J_{11} extracted from the simulation and the magnitude of J_{11} analytically computed from the data of the single layer. On the z axis is possible to appreciate that the simulated geometries are able to 0 to 2π phase range. **(b)** : Difference between the magnitude of J_{22} extracted from the simulation and the magnitude of J_{22} analytically computed from the data of the single layer. On the z axis is possible to appreciate that the simulated geometries are able to 0 to 2π phase range

3.2.3. Bilayer simulations: sweep of the dimensions of both bottom and top nanofin: the fractal metasurface

The last step performed was a simulation consisting in the sweep of both the dimensions of bottom and top nanofins. It was not possible to simulate the complete set of structures simulated in the previous steps since it would have implied a total number of structure to be simulated larger than 10^6 . As a consequence, decided to simulate the combination of 121 geometries per layer (each dimension could have 11 different values) for a total of 14641 different geometries. On the other hand, we choose to maintain the same mesh size to guarantee the highest possible accuracy. As a result, the simulation took almost a month to be completed on our supercomputer. Once we obtained the results of the simulation, we used Eq. (3.5) to understand if it is possible, in the most general case, to use the library of a single layer to compute the Jones matrix of a bilayer.

In Fig. 3.7 the results obtained from the product of the Jones matrix is shown: the Figure is a grid made of 121 subplots. The figure has to be interpreted as follows: each subplot represent the values of the Jones matrix of a bilayer whose bottom fin has dimension equal to the ones reported on the axis while the dimensions of the top nanofin are sweeping. In Fig. 3.8 it is possible to appreciate the results of the FDTD simulation: the meaning of the plot is the same described above but in this case the plots represent the results of the simulation and not the analytical product. From the figure it is possible to notice that, both for the analytical and the simulated case, the behaviour of each subplot resemble the behaviour of the whole plot like as it is for fractal objects.

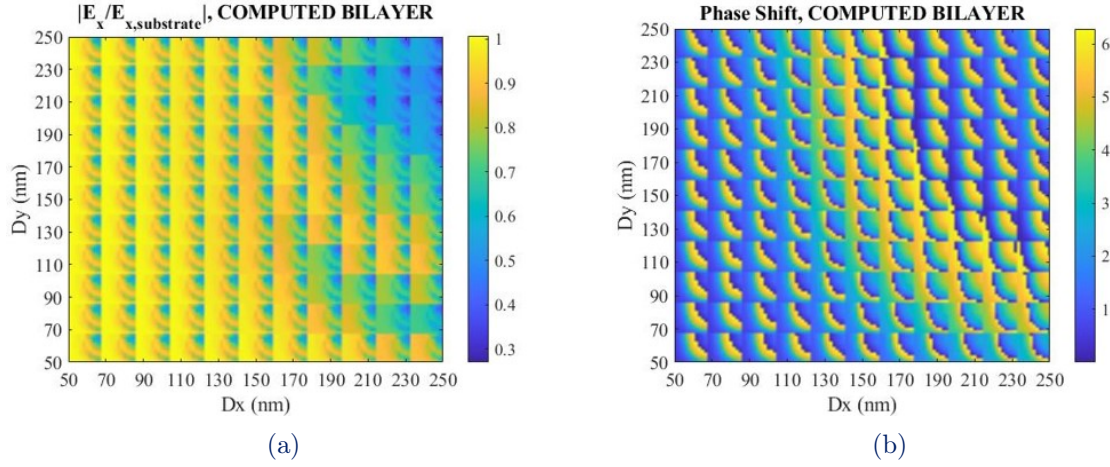


Figure 3.7: Plots of the analytical Jones matrix of a bilayer computed as the product of the Jones matrices of a single layer.: **(a)** : Plot of the analytical power transmission of a bilayer computed starting from the data a single layer. **(b)** : Plot of the analytical phase of a bilayer computed starting from the data a single layer.

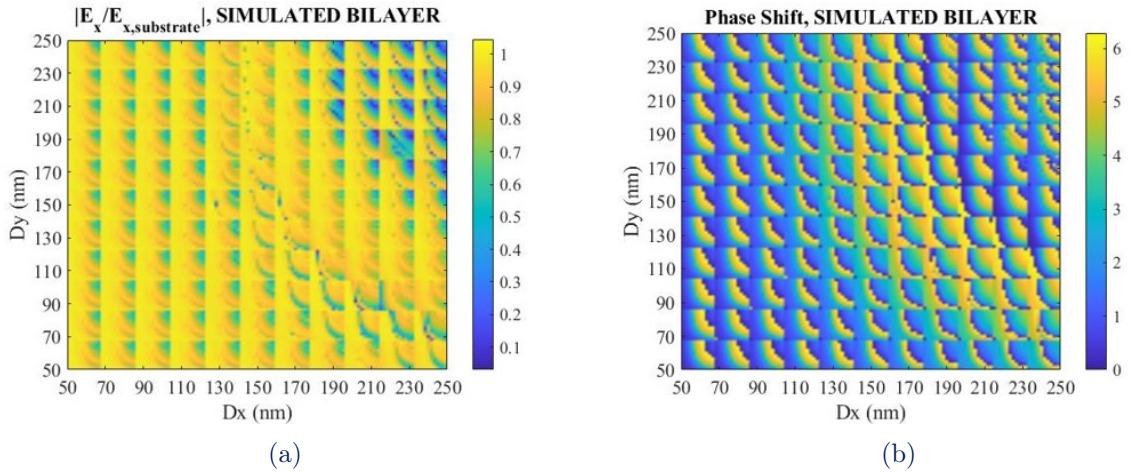


Figure 3.8: Plots of the analytical Jones matrix of a bilayer metasurface: **(a)** : Plot of the simulated power transmission of a bilayer metasurface. **(b)** : Plot of the analytical phase of a bilayer metasurface.

From Fig. 3.9 it is possible to look at the error between the simulated and the analytical cases. For the 70% of the simulated geometries the error in the phase is lower than the 10% in magnitude while for the 85% of the structures the error in the phase is lower than 15°. This analysis ensures the possibility to write the Jones matrix of a bilayer metasurface as the product of the Jones matrix of a single layer metasurface over this parameter

space. In order to get a reason of why some of the bilayer metasurface show a different behaviour from the one obtained using the analytical approach a different analysis needs to be performed. It is so possible to assert that for a large number of geometries the hypothesis of decoupling between the two layers can be considered as valid. The phase redundancy afforded by the metasurface library offers a sufficient number of decoupled geometries with full 2π phase coverage.

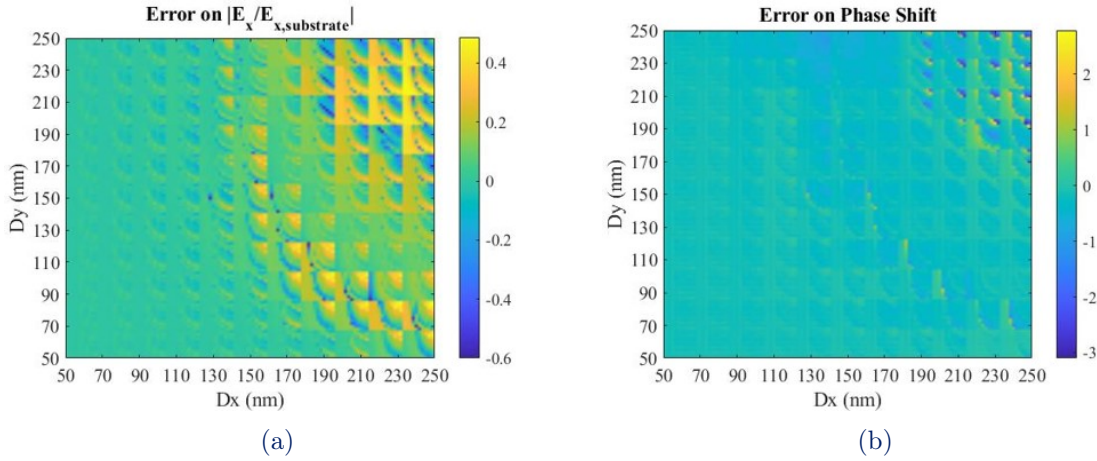


Figure 3.9: Plots of the error between the simulated Jones matrix of a bilayer metasurface and the analytical Jones matrix computed as product of Jones matrix of a single layer: **(a)** : Plot of the error in the power transmission of a bilayer metasurface. **(b)** : Plot of the error in the phase of a bilayer metasurface.

3.3. The bilayer metasurface in reflection

The previous analysis have shown that we can evaluate the Jones matrix of a bilayer working in transmission starting from the Jones matrix of a single layer metasurface. This allows the designer to build a bilayer metasurface by only making use of the single layer metasurface library, thereby, simplifying the design process. In this section, we investigate the possibility of writing the Jones matrix of a bilayer metasurface (Fig. 3.10) in reflection as the product of four Jones matrix of a single layer metasurface. The product of one element of the bilayer metasurface in case no rotation angle of the nanofins is introduced is given by:

$$\mathbf{J}_{\text{bilayer}} = \mathbf{J}_{\text{top}} \cdot \mathbf{J}_{\text{bottom}} \cdot \mathbf{M} \cdot \mathbf{J}_{\text{bottom}} \cdot \mathbf{J}_{\text{top}} \quad (3.6)$$

where \mathbf{M} is the Jones matrix of a mirror. As it can be seen from Eq. (3.6) the elements

of the product are 2 by 2 equal: the first two elements are related to the path that the light make when impinging on the metasurface and it passes thorough the two nanofins, then it is reflected by the mirror and so it passes through the two fins one again but this time, in the reverse order.

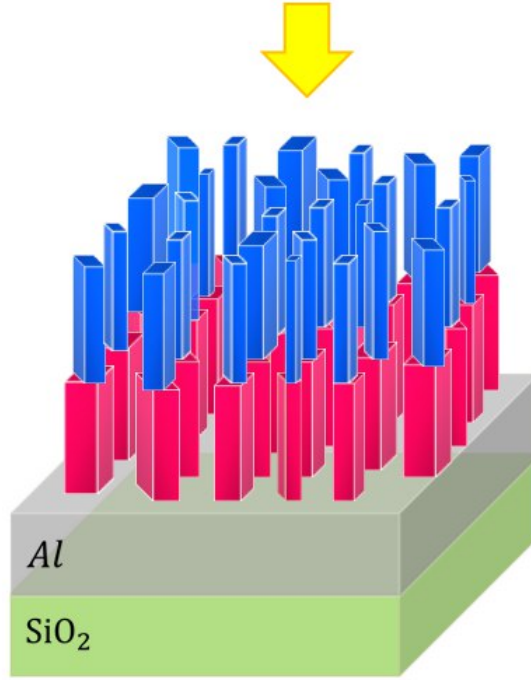


Figure 3.10: Model of a bilayer metasurface in reflection. The silver layer represents the mirror. The yellow arrow represents the incident light.

In order to test the validity of Eq. (3.6) we started by simulating a unit cell consisting of a single layer in reflection and then we move to the discussion of a bilayer metasurface in reflection presenting as an example a Pancharatnam–Berry phase-based bilayer metasurface.

3.3.1. Single layer metasurface in reflection

Following the same approach used in the previous section, we simulated a single layer metasurface in reflection in order to verify if, in presence of a mirror, it was possible to write the Jones matrix of the system as product as follows:

$$\mathbf{J}_{\text{bilayer}} = \mathbf{J}_{\text{top}} \cdot \mathbf{M} \cdot \mathbf{J}_{\text{bottom}} = \begin{bmatrix} e^{i\phi_{x,1}} & 0 \\ 0 & e^{i\phi_{y,1}} \end{bmatrix} \cdot \begin{bmatrix} 1 & 0 \\ 0 & -1 \end{bmatrix} \cdot \begin{bmatrix} e^{i\phi_{x,2}} & 0 \\ 0 & e^{i\phi_{y,2}} \end{bmatrix} \quad (3.7)$$

The unit cell (whose size is always $420\text{nm} \times 420\text{nm}$) simulated is the one shown in Fig. 3.11. The unit cell is illuminated with a plane x- polarized wave source at 532 nm that has been placed at a distance of 600 nm from the top of the basis of the nanofin. A 150nm thick Aluminum mirror has been place between the substrate and the nanofin: the refractive index of the Aluminium at the used wavelength has been set to $0.91 + i6.55$. A monitor has been placed a few wavelengths above the nanofins to collect the electric field that is reflected by the structure.

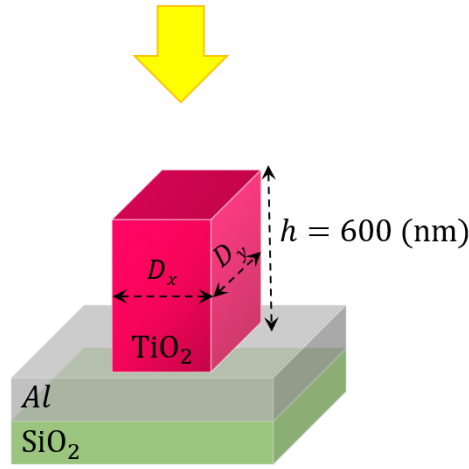


Figure 3.11: Unit cell of a single layer metasurface working in reflection mode. The silver sheet represent a 150nm thick Aluminum mirror. The structure is illuminated from the top as denoted by the yellow arrow.

The results of the simulation are shown in the (a)s of Fig. 3.12 and in Fig. 3.13. From Fig. 3.3b it is possible to appreciate the results analytically computed from the product of the Jones Fig. of a single layer in transmission. It is noticed that the new structure in reflection has both power transmission and phase shift completely different from the ones obtained from an analytical approach since in the reflection case some peculiar features arise from the simulation that could not be obtained from a simple product of Jones matrix. It can be assumed that, the interface between the mirror and the nanofin have changed the effective refractive index of the TiO_2 that result in a different response of the structure when illuminated. So it can be concluded that, differently from what happens in the case of the transmissive bilayer metasurface where in most of the cases the analytical approach is accurate enough to allow to use the data coming from the library of a reflective single layer metasurface, in the case of a single layer this can not be done. In order to reduce the error between the simulated case and the analytical approach we tried to modify the mirror matrix from the "standard" expression used in Eq. (3.7) with a Mirror

matrix that was able to reproduce the effect of an aluminum mirror but the reduction of the error was not so much. We also tried to optimize the mirror thickness varying it in a range between 10nm and 300nm but we found out that a mirror thickness of around 150 nm guarantee an average error similar to the other mirror thickness. So to reduce the error we modified the structure as it will be discussed in the next section.

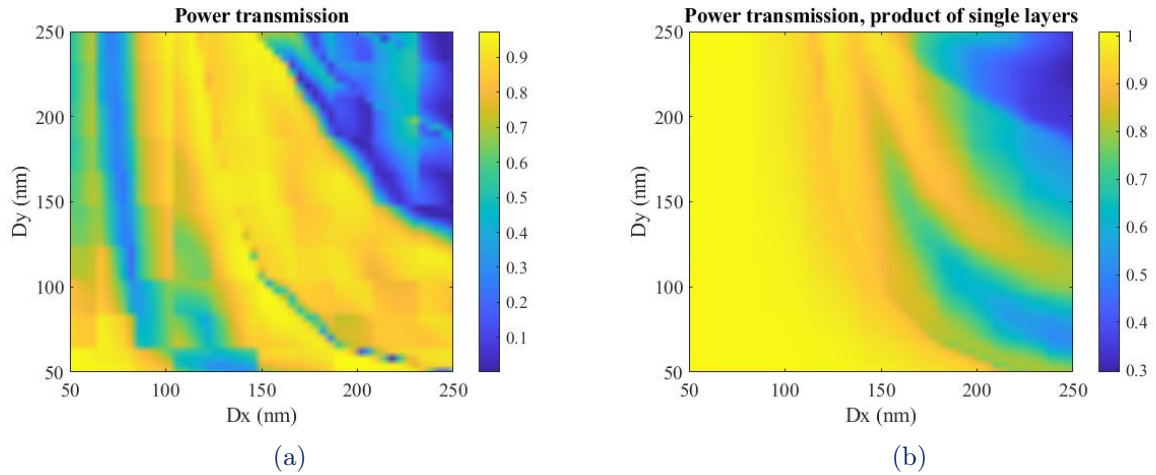


Figure 3.12: Comparison of the power transmission plots between a simulated single layer metasurface in reflection and the results obtained from the product of Jones matrix: **(a)** : Results of the simulation. **(b)** : Plot of the analytical power transmission.

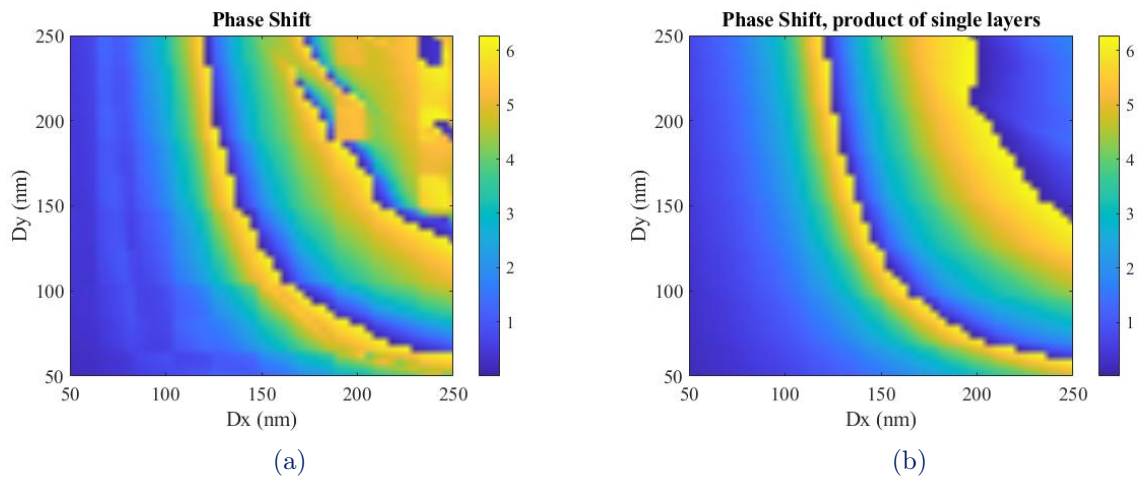


Figure 3.13: Comparison of the phase shift plots between a simulated single layer metasurface in reflection and the results obtained from the product of Jones matrix: **(a)** : Results of the simulation. **(b)** : Plot of the analytical phase shift.

3.3.2. The addition of a silica spacer in a single layer metasurface working in reflection

The strategy that we adopted in order to match the results analytically obtained from the product of the Jones matrix of a single layer in transmission we modified the structure inserting a silica spacer between the mirror and the nanofin. Since we assumed that the change of the refractive index of the TiO_2 fin was due to the interface between the mirror and the fin, the insertion of a spacer, whose dimension needs to be optimized, should be able to match the behaviour of the nanofin when working in transmission where it was in direct contact with the silica substrate. The unit cell of the new structure is shown in Fig. 3.14.

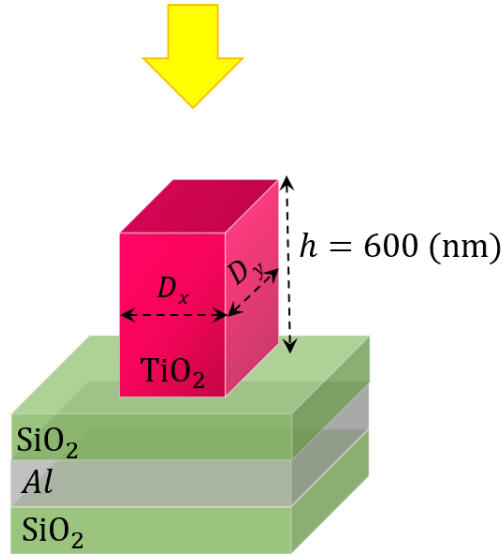


Figure 3.14: Unit cell of a single layer metasurface working in reflection mode with the addition of a silica spacer. The silver sheet represent a 150nm thick Alluminum mirror. The structure is illuminated from the top as denoted by the yellow arrow.

In order to optimize the space thickness we sweep the thickness of the spacer between 20nm and 160 nm and for each spacer thickness we sweep the dimension of the fin in the unit cell between 50nm and 250nm. Then for each fin geometry we selected the spacer dimension that was minimizing the difference between the phase difference between the analytical product of the Jones matrices of a single layer metasurface working in reflection and the results of the simulation with the optimized space thickness. In Fig. 3.15 it is shown the comparison between the analytical phase shift and the results of the space

selection method described above.

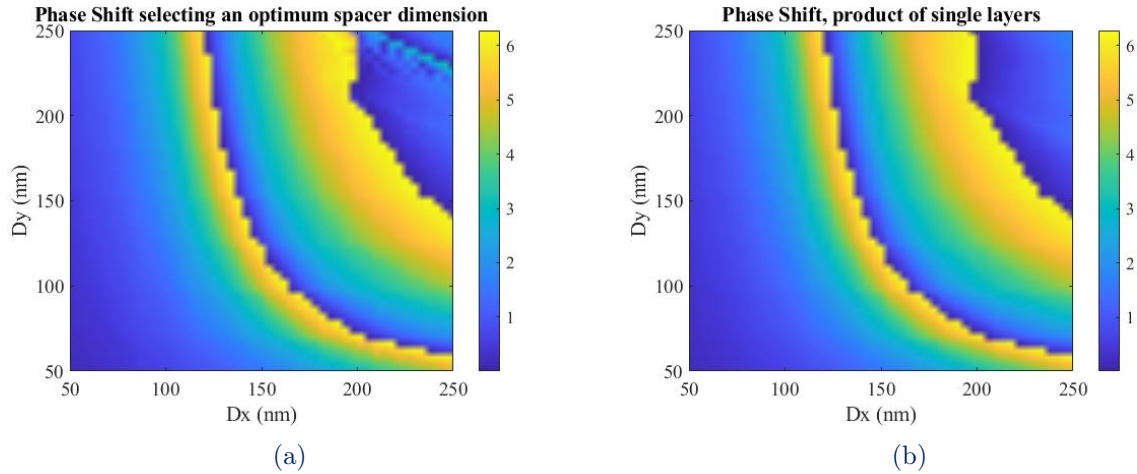


Figure 3.15: Comparison of the phase shift plots between a simulated single layer metasurface in reflection and the results obtained from the product of Jones matrix: **(a)** : Results of the simulation. **(b)** : Plot of the analytical phase shift.

As it can be clearly noticed from Fig. 3.15 the difference between the analytical approach and the simulation results selecting the optimum spacer thickness is reduced from the case where the spacer was not used (Fig. 3.13). So thanks to the addition of a spacer it is now possible to write also for the case of a single layer metasurface in reflection, its Jones matrix describing the structure as a product of the Jones matrix of a single layer metasurface. The validity of the analytical approach is confirmed looking at Fig. 3.16 where the errors of the power transmission and the phase shift are plotted. Since the selection rule of the spacer it is on the phase shift is can be seen that the error in the phase (Fig. 3.16a) is almost zero for all the structure (the error in the phase shift is lower than 3° for 95% of the cases) while it is on average bigger on the power transmission (Fig. 3.16b). The geometries that exhibit a larger error are the biggest in the simulated range: probably it would be needed to increase the spacer thickness to reduce the error also for these dimensions. It can be argued that the insertion of a given spacer dimension that optimize the response of a certain geometry will constrain to fabricate a metasurface that has always the same geometries so limiting the degrees of freedom of the system.

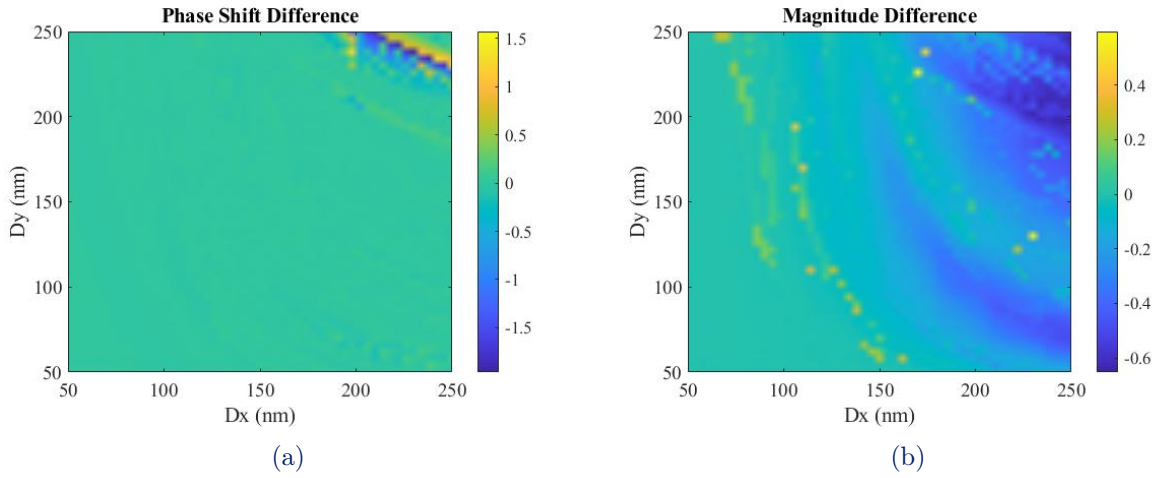


Figure 3.16: Plots of the error between the simulated Jones Matrix of a single layer metasurface in reflection and the analytical Jones Matrix computed as product of Jones matrix of a single layer in transmission. **(a)** : Plot of the error in the power transmission of a single layer metasurface in reflection. **(b)** : Plot of the error in the phase of single layer metasurface in reflection.

The figure of merit of this analysis is Fig. 3.17. The reported figure shows the optimum spacer thickness as a function of the nanofin dimensions. On the z axis the error in the phase is reported.

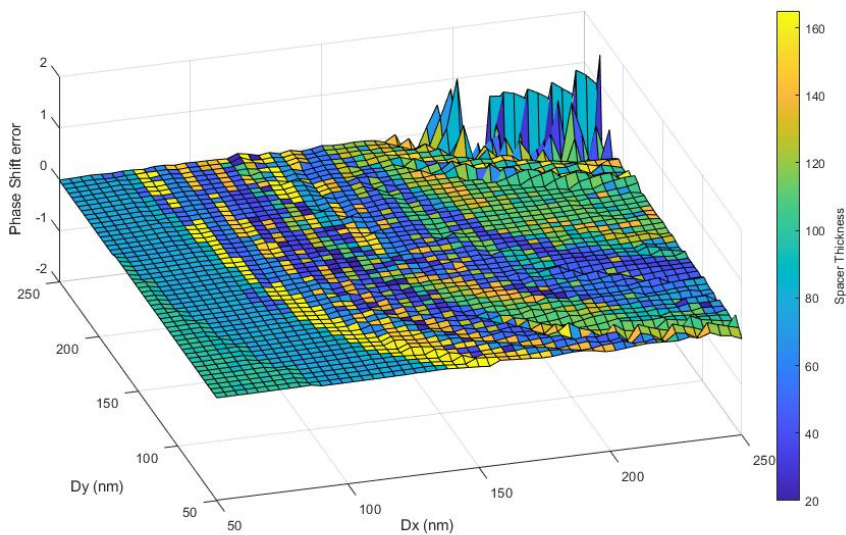


Figure 3.17: Optimum spacer dimension as a function of the nanofin geometry. On the z axis the error in the phase is reported.

3.3.3. Bilayer simulation: bottom fin fixed and sweeping of the top fin

To the aim of designing a bilayer metasurface in reflection we repeated the same analysis performed in transmission described in 3.2.2: we fixed the dimension of the bottom nanofin and we performed a parameter sweep of the dimensions of the top nanofin without introducing a rotation angle between the fins. The previous analysis on the spacer optimization was needed to select the spacer dimension that optimizes the response of the fixed bottom geometry. This allow us to verify the assumption of decoupling in reflection for all the geometries. We also confirm that the spacer dimension from the single layer is valid for the design of a bilayer metasurface in reflection; in which case the Jones matrix of the bilayer can be written as shown in Eq. (3.6).

The dimension of the bottom nanofin are the one of the QWP_1 : $134\text{nm} \times 202\text{nm}$. As a consequence for the bottom nanofin we used the Jones matrix of this element reported Table 2.1: this value will be the same for all the bilayers, independently from the dimensions of the top nanofin. From the previous analysis the optimized spacer thickness is set to 100nm . The simulated unit cell is shown in Fig. 3.18.

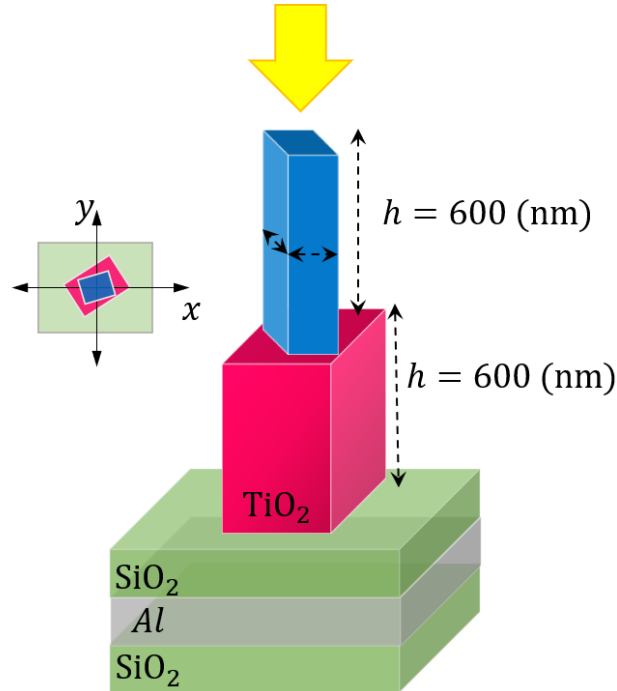


Figure 3.18: Unit cell of a bilayer metasurface working in reflection mode with the addition of a silica spacer. The silver sheet represent a 150nm thick Aluminum mirror. The structure is illuminated from the top. The yellow arrow represents the incident light.

Fig. 3.19 and Fig. 3.20 report the difference between the simulated case and the analytical approach. It can be noticed that the error is on average close to zero both for power and phase plots for both the Jones matrix elements. The phase error is lower than 5° for 81% of the cases for J_{11} and 88% of the cases for J_{22} . The cases that show larger errors are the ones composed by a top nanofin that is much larger than with respect to the bottom one. This can be due to the reflections that occur between the mirror and the base of the top nanofin. The spacer selection rule defined above allows to correctly design a bilayer metasurface working in reflection whose Jones matrix can be predicted starting from a simple library of a single layer metasurface working in transmission. It can be concluded so that, in order to design a bilayer metasurface working in reflection it is not needed to simulate a full library describing all the possible cases sweeping the dimensions of the bottom and the top nanofin but it is sufficient to start from a library describing a single layer metasurface working in transmission (that is much less computational intensive) and to select the optimum spacer thickness according to the selection rule described above whose results are shown in Fig. 3.17.

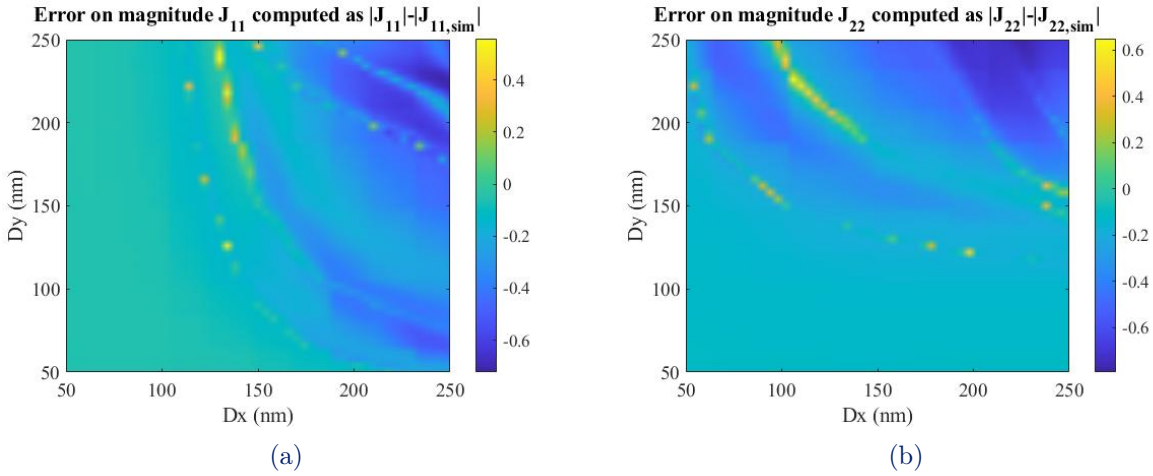


Figure 3.19: Plots of the difference in magnitude between the Jones matrix elements of the simulated bilayer in reflection with bottom fin fixed and the Jones matrix elements of a bilayer analytically computed: **(a)** : Difference between the phase of J_{11} extracted from the simulation and the phase of J_{11} analytically computed from the data of the single layer. **(b)** : Difference between the phase of J_{22} extracted from the simulation and the phase of J_{22} analytically computed from the data of the single layer.

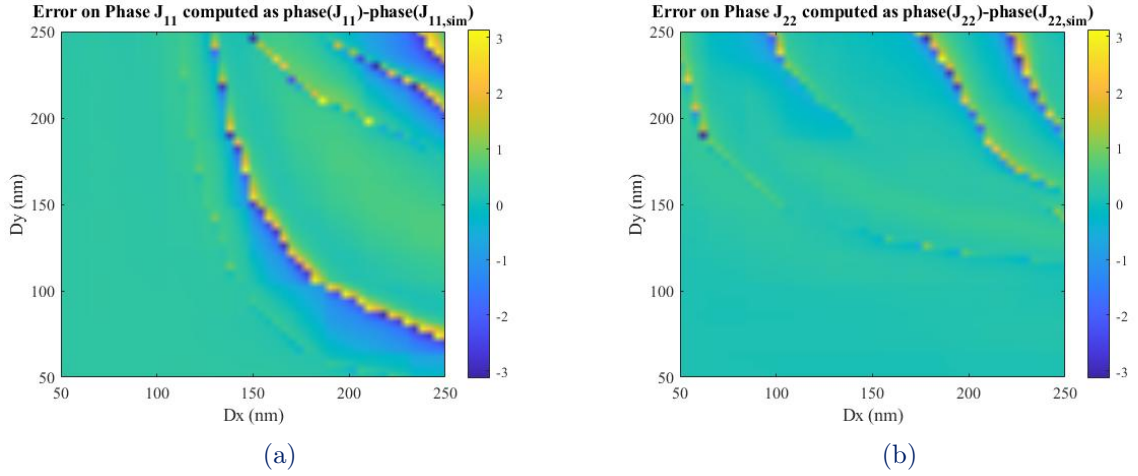


Figure 3.20: Plots of the difference in magnitude between the Jones Matrix elements of the simulated bilayer in reflection with bottom fin fixed and the Jones matrix elements of a bilayer: **(a)** : Difference between the magnitude of J_{11} extracted from the simulation and the magnitude of J_{11} analytically computed from the data of the single layer. **(b)** : Difference between the magnitude of J_{22} extracted from the simulation and the magnitude of J_{22} analytically computed from the data of the single layer.

3.4. A Pancharatnam–Berry phase-based bilayer metasurface

On the basis of the analysis discussed up to now, here we show a possible application a bilayer metasurface in reflection. In analogy to the case of single layer metasurface, we present a Pancharatnam–Berry phase bilayer metasurface that, thanks to the larger number of degree of freedom that this metasurface enables, allows to work on linear polarization and not only on circularly polarized light as it was with single layer metasurfaces. In [40] a Michelson interferometer like system (Fig. 3.21) consisting of two quarter waveplates and a mirror on one arm and a single mirror in the other arm of the interferometer is designed in order to take advantage of the geometric phase accumulation to shift the frequency of the impinging light beam.

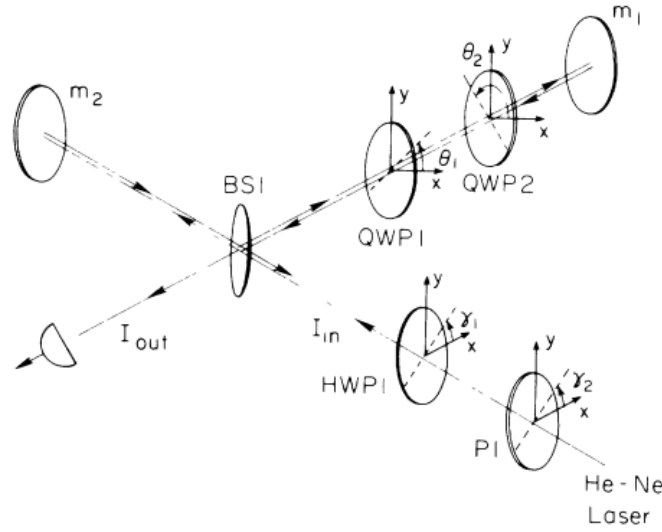


Figure 3.21: Experimental arrangement for the generation of a time-varying geometric phase. The basic configuration is that of a Michelson interferometer. Figure from [40]

Each quarter wave plate will act as a rotation through $\pi/2$ about an axis in the equatorial plane of the Poincare sphere. A rotation of the quarter-wave plate (about the z axis normal to the plate) by θ would rotate this equatorial axis by 2θ . If we consider light polarized along the x axis incident on a quarter-wave plate whose slow axis makes an angle of $\pi/4$ with the x axis. The emergent light which is left circularly polarized then passes through a second quarter wave plate whose slow axis makes an angle of $3\pi/4 + \phi$ with the x axis. The incident light is represented by the point X on the Poincare sphere, the light emerging from the first quarter-wave plate by LCP, and that from the second quarter-wave plate by the linear polarization state A . This light falls normally on a plane mirror and after reflection passes back through the two quarter wave plates. The polarization state is transformed from A to RCP and then to X as shown in Fig. 3.22a. For y -polarized light the evolution is again cyclic, but given by the reflection of this circuit through the origin (Fig. 3.22b). Clearly, the two circuits are traversed in opposite senses; and hence subtend equal and opposite solid angles at the origin equal to 4ϕ and as a consequence a Berry phase of $\pm 2\phi$ will be acquired respectively from x and y polarization. In the article the second quarter wave plate is rotated uniformly so that the geometric phase changes linearly in time contributing to a shift in frequency. Here we present a static device: a bilayer metasurface grating whose principle is similar to the structure described in [40].

From the library shown in Fig. 2.2 we selected two nanofins whose Jones matrix is the one of a quarter wave plate. Among the possible structure that behaves as quarter wave plates we choose the \mathbf{QWP}_1 ($134 \text{ nm} \times 202 \text{ nm}$) to be the bottom nanofin and the

QWP_2 ($114 \text{ nm} \times 154 \text{ nm}$) to be the top nanofin of a bilayer metasurface working in reflection. The analysis previously discussed allows to consider these two nanofins as decoupled and guarantee that they behave as quarter waveplates also when being part of a bilayer metasurface in reflection. When x-polarized light impinges on the system, as it was for the interferometer described above, the top nanofin (that is a quarter wave plate), it will be transformed to left circularly polarized light that, going through the bottom nanofin, will be transformed into linearly polarized light again. After the reflection of the mirror, the polarization will be transformed respectively into right circularly polarized light after the bottom nanofin and back to x-polarized light after the top nanofin. A closed path on the Poincaré sphere, shown in Fig. 3.22, as it was for the interferometer, will be then traced. For y-polarized light the evolution is again cyclic, but given by the reflection of this circuit through the origin. By introducing a relative rotation between the nanofins it will be also possible to vary the path on the Poincaré sphere so that the solid angle subtended by the path will change accordingly to the relative rotation angle.

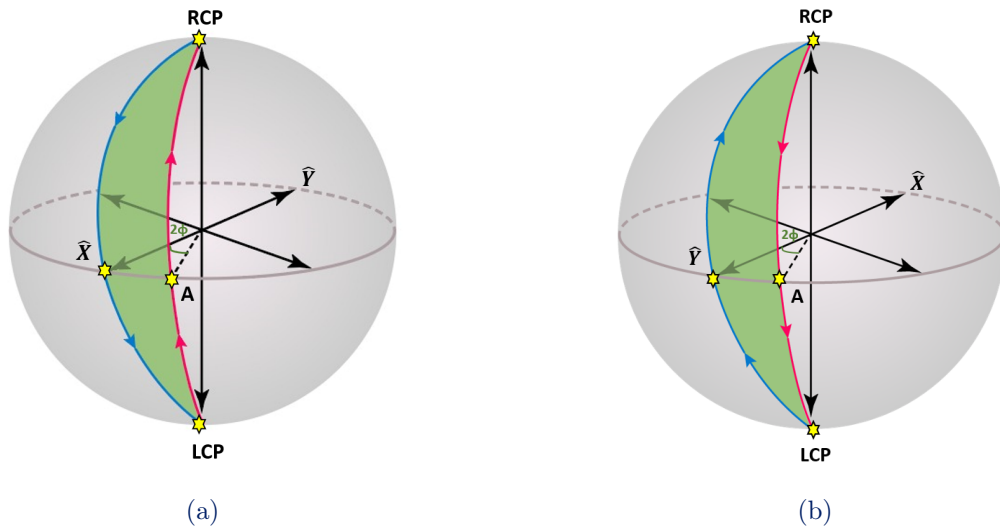


Figure 3.22: Evolution of polarization on the Poincaré sphere: starting from x-polarized light, passing through the top nanofin, polarization will be transformed into LCP. Then going through the bottom nanofin we go from LCP to point A that depends on the relative rotation between the two nanofins. Light is then reflected by the mirror it goes through the bottom nanofin again going from A to RCP and then, thanks to the second nanofin, from RCP back to X. Polarization transformations due to the top nanofin are represented by the blue arrows while transformations due to the bottom nanofins are represented by the pink arrows. For y-polarized light the evolution is again cyclic, but given by the reflection of this circuit through the origin. (a) : Incident x-polarized light. (b) : Incident y-polarized light.

So, depending on the rotation angle, that is internal geometric parameter, and consequently on the solid angle, light will acquire a phase factor that is nothing else than the Pancharatnam–Berry phase. On this basis we designed a simple grating (Fig. 3.23) consisting of 24 unit cells each one containing a bilayer structure: between the two fins a rotation angle is introduced and the rotation spatially varies from 0° to 360° with a step of 15° . What we expect is that, depending on the incident beam that is x or y-polarized, the light will be scattered into the +1 or -1 diffracted order.

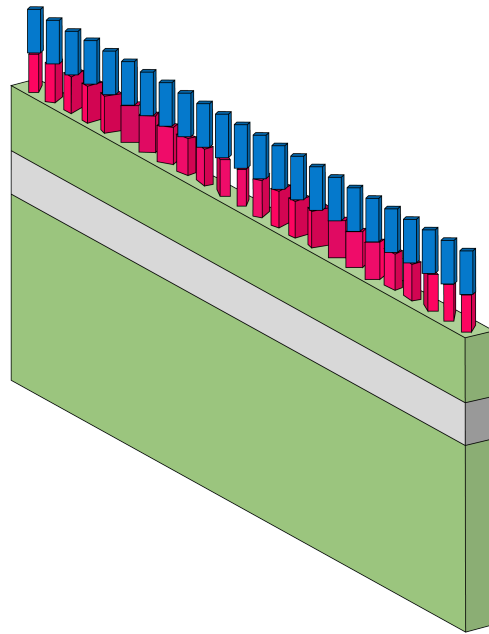


Figure 3.23: Model of the designed grating.

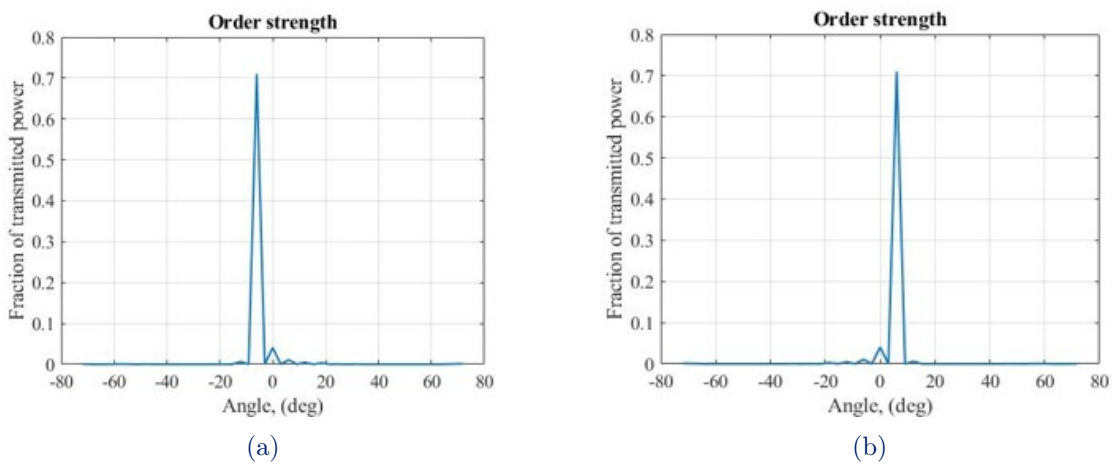


Figure 3.24: Fraction of transmitted power as a function of diffracted angle: (a) : X polarized incident beam. (b) : Y polarized incident beam.

From the Fig. 3.24 it can be seen that only a small fraction of the input energy appears in the zeroth order with a diffraction efficiency of 80%. As expected, when the incident polarization is linear, the two orthogonal components of the beam are subject to different diffractive geometric phase (that arise due to the different path on the Poincaré sphere) of opposite sign and are diffracted to first order in different directions (-1 for x-polarized light in Fig. 5.17a and $+1$ for y-polarized light in Fig. 5.17b). To conclude, we have demonstrated a bilayer metasurface application: a polarization-dependent optical bilayer metasurface based on the Pancharatnam–Berry phase. In contrast to the system from the system described in [40], our metasurface is a static device, so, once the device has been fabricated, it is not possible to rotate one of the two fins to obtain a frequency shift. A non static device that offers the possibility to tune phase, amplitude or polarization of an optical wavefront will be discussed in the next section: the Spatial Light Modulator.

4 | Dynamic wavefront shaping with SLMs

Spatial light modulators (SLMs) refer to a number of devices that allow to modify phase, amplitude or polarization of an optical wavefront as a function of position across the wavefront. These devices can be reconfigured in real time electrically (computer-controlled) or optically (optical addressing). In this section we provide an introduction to these devices and we describe the polarization transformation attainable with cascades of several SLMs.

4.1. Principle and application of SLMs

Spatial light modulation can be achieved through a plethora of technologies such as mechanically or thermally deformable mirrors [41], magneto-optic devices or acoustic-optic Bragg cells [42], or liquid crystals (LCs). The latter are organic materials characterized by physico-chemical proprieties between those of liquids and solids, enabling the possibility to locally change the phase of the propagating readout light. Elongated LC molecules therefore have both a structural order and anisotropy specific to crystals such as optical, dielectric or even elastic anisotropy; at the same time the existence of a liquid order allows to tune the proprieties of LCs. The application of an electric field results in the creation of elastic forces leading to the reorientation of the molecules that tend to line up in the direction where the strain energy is minimal and the intensity of the electric field modulates the molecular orientation. Spatial control of the applied electric field, pixel by pixel, offers the ability to spatially modulate the phase of an incident optical wave. This effect can be either used as a pure phase modulator (if the incident polarization is always linearly polarized along the bias-tunable axis) or as a pure-amplitude modulator (if the LC cell is placed between analyzers that may be crossed or parallel, depending on the exact implementation, as in LC displays).

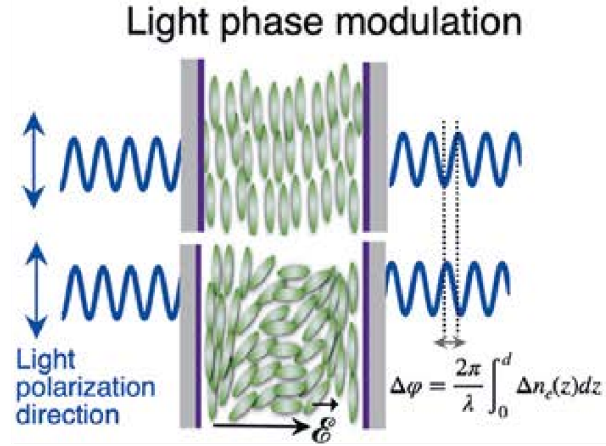


Figure 4.1: Liquid Crystal Spatial light modulator: when an electric field is applied, the orientation of the molecules changes so that the optical refractive index changes and the phase of a propagating light is modified accordingly. Figure from [43]

4.2. Polarization-Transformations with Systems of Multiple SLMs

SLMs based on liquid crystals are among the most common and widely used, especially those integrated on silicon with CMOS drive electronics. Cascades of LC SLMs enable the possibility to spatially modulate polarization as it has been described in [44]. As it is for metasurfaces, an SLM can be described by a spatially varying Jones matrix:

$$\mathbf{J}(x, y) = \begin{bmatrix} e^{i\phi_x(x, y)} & 0 \\ 0 & 1 \end{bmatrix} \quad (4.1)$$

since each pixel of the SLM can be seen as a tunable retarder and where $\phi_x(x, y)$ is the phase shift on linear x-polarized light that can be tuned. In order to obtain the same control over y-polarized light rotating an SLM by 90 so cascading two SLMs a diagonal Jones matrix can be obtained. However, cascading two SLMs it is not possible to obtain a Jones matrix of the form of Eq. (1.12) since the pixel of the SLM cannot be individually and independently rotated as it is for the nanofins of dielectric metasurfaces. In order to implement the rotation matrix $R(\theta)$ it is necessary to sandwich the SLM between two quarter-wave plates, oriented at $\pm 45^\circ$. The first quarter wave plates converts the incoming light into the circular basis that is retarded along one polarization by an angle that the SLM can control spatially, and converted back to its original basis by the second quarter wave-plate. If a cascade of two SLM (that implements a diagonal Jones matrix),

is sandwiched between the latter described system (Fig. 4.2), it is possible to obtain a Jones matrix of the form (1.12) that can be realized with a single layer metasurface. The advantage of using SLM with respect to metasurface is the electrical, computer-addressed tunability of the SLM with respect to metasurfaces that are static devices albeit at much lower resolution.

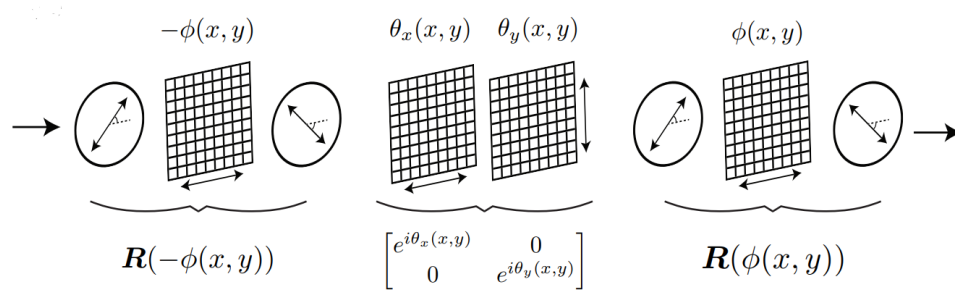


Figure 4.2: Implementation of spatially varying polarization control with configurations of spatial light modulators (SLMs). Figure from [44]

5 | A new degree-of-freedom of light: Rotatum

In this chapter, we study a popular class of structured light known as vortex beams, which carry orbital angular momentum (OAM). Using a spatial light modulator, we control the OAM of those beams following a step-like, linear, and quadratic evolution along their optical path. The latter yields a new property of light that we refer to as the "optical rotatum". We also show that the continuous evolution of OAM is associated with a perturbation in the longitudinal component of the wave vector that is connected to the Pancharatnam-Berry phase.

5.1. Frozen waves

The existence and the proprieties of localized waves have been well known for a long time being introduced in [45]. These particular waves have the peculiarity to being able to resist to diffraction for a long distances.e., of possessing a large depth of field. The most popular among the possible localized waves is the Bessel beam. If Bessel beams with the same frequency, but with different longitudinal wave numbers are superimposed, it becomes possible to control the beam intensity longitudinal shape within a chosen interval so that the intensity envelope remains static, i.e., with velocity $v = 0$ [46]. This peculiar superposition of Bessel beams is generally known as "Frozen wave".

5.1.1. Mathematical formalism of Frozen waves

A possible solution of the Helmolzt equation is given by the zeroth-order Bessel beam:

$$\Psi(\rho, z, t) = J_0(k_\rho \rho) e^{ik_z z} e^{-i\omega t} \quad (5.1)$$

where ω , k_ρ and k_z are respectively the angular frequency, the transverse and longitudinal wave number that must satisfy:

$$k_\rho^2 + k_z^2 = \frac{\omega^2}{c^2} \quad (5.2)$$

The superposition of $2N + 1$ Bessel beams with the same frequency and different longitudinal wave numbers can be written as follows:

$$\Psi(\rho, z, t) = e^{-i\omega t} \sum_{n=-N}^N A_n J_0(k_{\rho_n} \rho) e^{ik_{n,z} z} \quad (5.3)$$

Equation (5.3) defines the "Frozen Wave". For each n , Eq. (5.2) must be satisfied. Supposing that, in a certain interval ($0 < z < L$) we want that

$$|\Psi(\rho, z, t)|^2 = |F(z)|^2 \quad (5.4)$$

where $F(z)$ can be expanded in Fourier series as:

$$F(z) = \sum_{m=-\infty}^{+\infty} B_m e^{i\frac{2\pi}{L} m z} \quad (5.5)$$

it is necessary to determine the values of $k_{z,n}$ and A_n in Eq. (5.3) so that

$$\left| \sum_{n=-N}^N A_n e^{ik_{n,z} z} \right|^2 = |F(z)|^2. \quad (5.6)$$

This problem can be solved selecting a $Q > 0$ and so that k_z can be written as

$$k_{z,n} = Q + \frac{2\pi}{N} n \quad (5.7)$$

and as a consequence A_n can be obtained as:

$$A_n = \frac{1}{L} \int_0^L F(z) e^{-i\frac{2\pi}{L} n z} dz \quad (5.8)$$

The exposed methodology and theory regarding frozen waves enables the possibility to control over the longitudinal direction, the intensity pattern (Fig. 5.1) in a certain region both in nonabsorbing [47] and absorbing media [48]. In [49] it is shown the possibility to change the intensity profile of a Frozen Wave over time. Frozen waves are at the foundation to a manipulation technique used to control the topological charge (sign and

magnitude) along the propagation direction [50] that is at the basis of the method here presented.

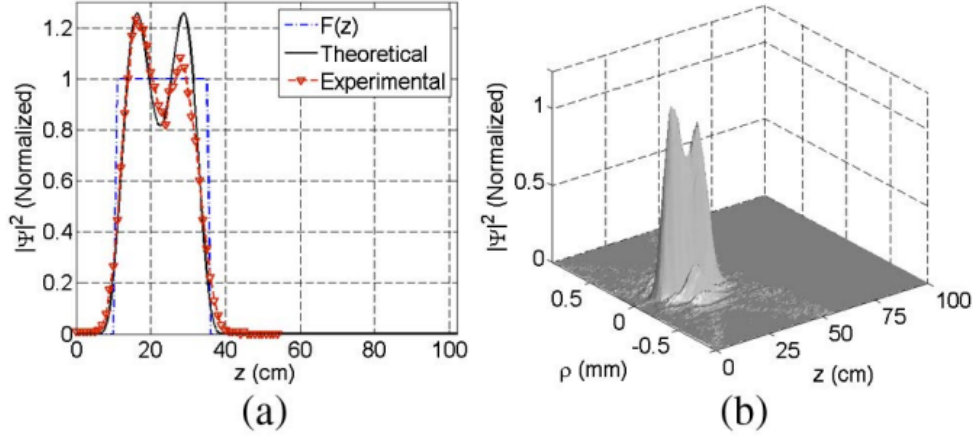


Figure 5.1: (a) Comparison of desired longitudinal intensity function (blue line), theoretical prediction by $\Psi(\rho, z)$ (black line), and experimental result (red line) for a step function; and (b) 3D plot of experimental intensity. Figure from [47]

5.2. Orbital Angular Momentum

Definition and generation of OAM beams

An important example, of fundamental and practical interest, has been light beams structured to carry orbital angular momentum (OAM). In 1992, Allen et al. highlighted that light beams with an azimuthal phase dependence of $e^{i\ell\phi}$ carry an orbital angular momentum (OAM) [51]: the OAM is a completely distinct quantity with respect to SAM (spin angular momentum of $\pm\hbar$ per photon) associated to circularly polarized light. Referring to classical mechanics a simple relationship can be established between linear ($\mathbf{p} = m\mathbf{v}$) and angular momentum \mathbf{L} :

$$\mathbf{L} = \mathbf{r} \times \mathbf{p} \quad (5.9)$$

where \mathbf{r} is the position of the particle. The first time-derivative of the angular momentum \mathbf{L} is the torque $\tau = \frac{d\mathbf{L}}{dt}$, while the second order time-derivative is known as rotatum. The simplest possible example of an OAM beam is one with a phase in the transverse plane of $\phi(r, \phi) = e^{i\ell\phi}$, where ϕ is the angular coordinate and the variable ℓ , known as topological charge, can be any integer value, positive or negative. As it can be seen looking at (Fig. 5.2), light beams described by $\phi(r, \phi) = e^{i\ell\phi}$ have an helical phase front:

the number of helices depends on the magnitude of ℓ while their handedness depends on the sign of ℓ . It can be clearly seen that if ℓ is different from zero, the Poynting vector, which is parallel to the surface normal of the phase fronts, has an azimuthal component around the beam and hence an angular momentum along the beam axis. As it was pointed out in [52], the Poynting vector forms an angle of $\frac{\ell\lambda}{2\pi r}$ with respect to the beam axis and as a consequence the value of the azimuthal component of the light's linear momentum is $\frac{\hbar k_0 \ell \lambda}{2\pi r}$ per photon. From Eq. (5.9) it follows that the OAM can assume only values of the form $\ell\hbar$ and so it is quantized.

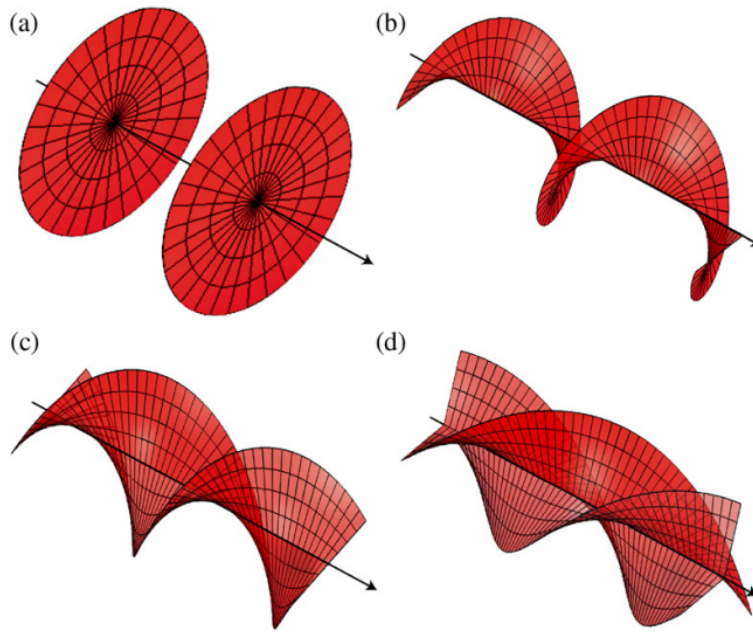


Figure 5.2: Helical phase fronts for (a) $\ell = 0$, (b) $\ell = 1$, (c) $\ell = 2$, and (d) $\ell = 3$. . Figure from [53]

The easiest way to generate an OAM beam with the peculiar helical phase fronts is to use of an optical element with a helical surface whose thickness varies along the azimuthal component that is $\frac{\ell\hbar\theta}{2\pi(n-1)}$ where n is the refractive index [54]. OAM can be also obtained using diffractive optical elements: combining a linear phase ramp and the the phase distribution of the desired optical component creates a forked diffraction grating that is able to produce a helically phased beam in the first diffraction order [55]. The components are effectively holograms of the desired optical element and are thus often referred to as “computer generated holograms” (CGH). This holographic technique can be implemented thanks to spatial light modulators (SLM) that can be programmed to acts as holograms.

5.2.1. Superposition of OAM beams

The superposition of these OAM beams allows to produce a nonrotationally symmetric intensity patterns that rotate at a constant angular velocity[56]. The superposition of two OAM beams with opposite topological charge ($\ell_1 = \ell_2$) and different propagation constant it can be obtained that the phase dependence is given by;

$$e^{i(\ell\phi - z\Delta k_z)} + e^{-i(\ell\phi - z\Delta k_z)} \propto \cos(\ell\phi - z\Delta k_z) \quad (5.10)$$

As a consequence, the angular velocity computed as the derivative along the propagation direction of the the orientation of the intensity profile $\Phi(z) = \frac{z\Delta k_z}{\ell}$ is constant and has no angular acceleration ψ :

$$\frac{d\Phi}{dz} = \frac{\Delta k_z}{\ell} \quad (5.11)$$

The zero angular acceleration ψ is a direct consequence of the linear variation in the phase profile as a function of the azimuthal angle. A periodic phase profile would instead produce an angular acceleration ψ of the form:

$$\psi(\phi) = \ell\phi + \cos(\ell\phi) \quad (5.12)$$

that has a non zero second derivative. In [57] it is shown that, taking advantage of digital holograms, it is possible to continuously tune the angular acceleration of these fields that can be engineered to extend over arbitrarily long distances.

5.3. Evolution of orbital angular momentum using frozen waves: step-like OAM transition

As it was reported in [50] it is possible to take advantage of the properties of frozen wave to dynamically control the topological charge with propagation direction. The evolution of the topological charge can be obtained from the superposition of frozen waves (ψ_ℓ) expressed as:

$$\Psi(\rho, \phi, z, t) = \sum_{\ell=-\infty}^{+\infty} \psi_\ell = e^{-i\omega t} \sum_{\ell=-\infty}^{+\infty} \sum_{m=-N}^{+N} A_{\ell,m} J_\ell(k_\rho \rho) e^{i\ell\phi} e^{ik_{z,\ell,m}z} \quad (5.13)$$

where, differently from Eq. (5.1), here the $2N+1$ Bessel beams are not of order zero but of order ℓ . The real part of the longitudinal wave number $k_{z,\ell,m}$ has the form of Eq. (5.7) and must satisfy for each Bessel beam Eq. (5.2). The imaginary part of the longitudinal wave number is expressed as $Im\{k_{z,\ell,m}\} = \frac{n_r n_i}{Rek_{z,\ell,m}}$, where n_r and n_i are respectively the real and imaginary part of the index of refraction of an arbitrary medium. The complex coefficients $A_{\ell,m}$ in Eq. (5.13) representing the weighting factors for the Bessel beams in the superposition have the same form expressed in Eq. (5.8). The key to control the topological charge in the longitudinal direction is given by the possibility to modify the morphological function $F_\ell(z)$ at will so allowing to select which frozen waves can contribute effectively to the beam center over a finite space interval and which frozen waves needs to be dispersed over a larger space in the outer rings of the beam so that they do not contribute to the topological charge of the beam center in that interval. It should be noticed that this evolution of the OAM does not violate the conservation of the orbital angular momentum: the outer ring of the Bessel beams composing the Frozen wave act as an OAM reservoir and can be restored at further propagation distance to the central ring so that the global OAM of the beam is preserved. The presented methodology allows to obtain a step-like transition so we replicated the results shown in [58]. In order to obtain a topological charge transition from $\ell = 1$ to $\ell = 2$ we defined two Frozen waves as superposition of 13 ($2N+1$ with $N=6$) Bessel beams. The value of Q is set to $0.9999925 \frac{2\pi}{\lambda}$. The value morphological function $F_\ell(z)$ associated with each Frozen wave mode ϕ_ℓ was defined as:

$$F_\ell(z) = \begin{cases} F_1 = 1 & 0cm \leq z < 10cm \\ F_{-1} = 1 & 10cm \leq z < 20cm \\ F_{-1} = F_1 = 0 & elsewhere \end{cases} \quad (5.14)$$

Once the morphological function $F_\ell(z)$ is defined, it is possible to obtain the coefficients according to Eq. (5.13) and so the complete expression of the frozen waves from Eq. (5.13). The results of the simulation are shown in Fig. 5.3.

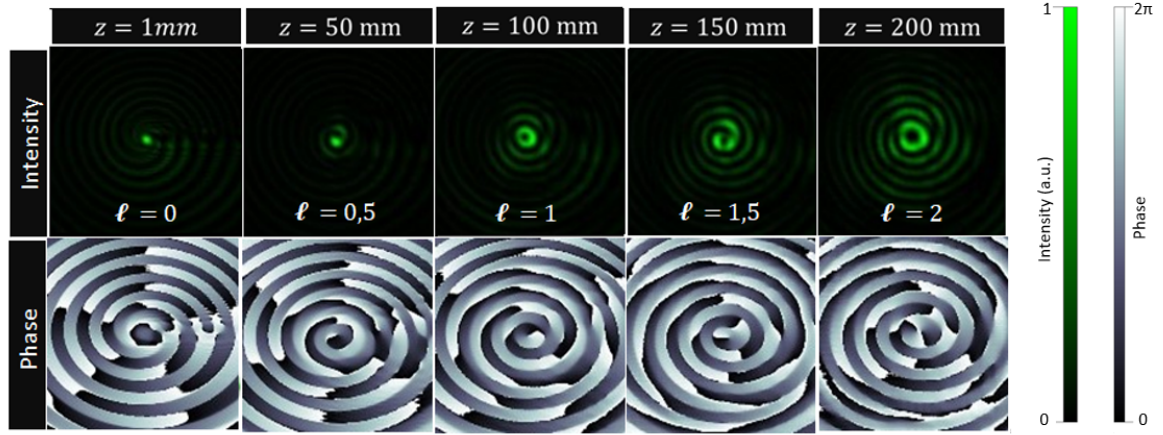


Figure 5.3: Simulated intensity (top row) and phase (bottom row) of the beam evolving its topological charge from $\ell = 1$ to $\ell = 2$ with a step-like transition. Phase and intensity profiles obtained at propagation distances: $z = 0$ cm, $z = 5$ cm, $z = 10$ cm, $z = 15$ cm, and $z = 20$ cm.

From the plots of the intensity and phase reported in Fig. 5.3 it can be noticed that the topological charge evolves along the propagation direction. The OAM, in the paraxial regime, can be computed starting from the ratio of angular momentum to energy per unit length of the beam whose expression is given by:

$$\frac{J_z}{W} = \frac{\int \int r dr d\phi (r \times \langle \mathbf{E} \times \mathbf{B} \rangle)_z}{c \int \int r dr d\phi \langle \mathbf{E} \times \mathbf{B} \rangle_z} = \frac{\ell}{\omega} \quad (5.15)$$

Calculating the OAM from Eq. (5.15), Fig. 5.8 shows its value as a function of z , the propagation direction. From the figure it can be noticed that the transition between the two values of two topological charge is sharp: the OAM does not increase continuously along the propagation direction but around $z = 10$ cm it goes from $\ell = 1$ to $\ell = 2$. The transition could have been also sharper if an higher number of Bessel beams was used to build the frozen wave.

The method that will be presented in the next chapter will allow instead to vary continuously along the propagation direction the value of topological charge.

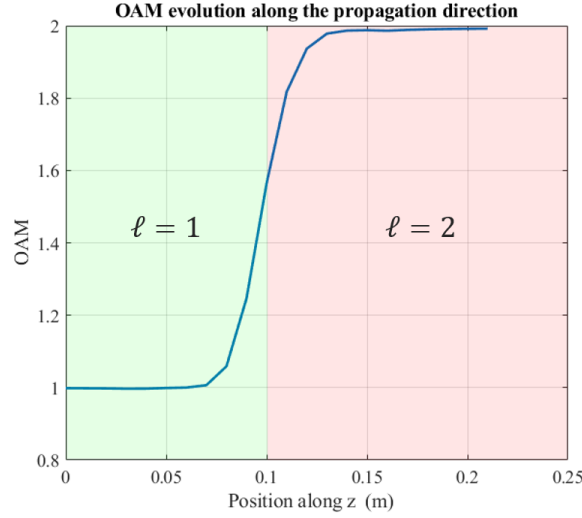


Figure 5.4: OAM evolution along the propagation direction. Step-like transition. Result of the simulation.

5.4. Continuous variation of topological charge along the propagation direction

The idea at the basis of the proposed method is the possibility to add a phase factor in the complex coefficient expression $A_{\ell,m}$, and in particular in the expression of the morphological function $F_{\ell}(z)$. In this method is necessary to use zero order Bessel beams constituting the frozen wave according to the formula reported in Eq. (5.1) differently from the step-like transition where it was needed to set two different frozen waves constituted by Bessel beams of different orders. The expression of the complex coefficient is given by:

$$A_{\ell,m} = \frac{1}{L} \int_0^L F_{\ell}(z) e^{-i(\frac{2\pi}{L}m)z} dz \quad (5.16)$$

and now we modify the expression of the morphological function so that it can be written as:

$$F_{\ell}(z) = e^{i\ell(z)\Phi} \quad (5.17)$$

The expression in Eq. (5.17) allows to control the phase evolution of the beam through the definition of an appropriate function $\ell(z)$. It is so possible, depending on the function $\ell(z)$ to add a degree of freedom that is related to how the topological charge is evolving in space. In the case $\ell(z)$ is linear, it is possible to tune the slope of the evolution that is nothing else than the first derivative of the angular momentum and so, it is pointed out

in the previous charge, to the the spatial analogous of Self-Torque τ . The Self-Torque, as light degree of freedom has been only recently "discovered" in [59] where time evolving OAM beams exhibit a time-dependent angular momentum that called self-torque. In the case $\ell(z)$ is parabolic is it possible not only to control the light self-torque but a new degree of freedom is introduced since it is possible to tune also the second derivative of the orbital angular momentum that, being the function $\ell(z)$ parabolic, will be non-zero. In analogy with classical mechanics, as it was for the spatial analogues of the self-torque, we named this new light degree of freedom as "Rotatum". In the following we report the simulation and experimental results obtained both or a linear and a parabolic $\ell(z)$.

5.4.1. Linear evolution of OAM

In order to obtain a linear variation of the topological charge along the propagation direction the expression of the morphological function $F_\ell(z)$ is the following:

$$F_\ell(z) = e^{i10\Phi z} \quad (5.18)$$

The coefficient 10 is necessary to obtain a integer value of the topological charge every 10cm. As it has been clarified the order of the Bessel beams constituting the Frozen wave has to be set to zero $\ell = 0$ so from now one, the index ℓ will be not reported. The values of the coefficient A_m is computed from Eq. (5.16):

$$A_m = -\frac{e^{2\phi i - (\frac{4}{5})i - i}}{5\phi - 2\pi m} \quad (5.19)$$

The results of the simulation are shown in Fig. 5.5. From Fig. 5.5 it can be noticed that, differently from the case reported in Fig. 5.3, both phase and intensity evolves continuously from $\ell = 0$ at $z=0$ to $\ell = 2$ at $z=20$ cm. The main differences can be noticed at the "intermediate" distances ($z=5$ cm and 15 cm) where both the amplitude and the phase have not the characteristic shapes of OAM exhibiting an integer topological charge while at these distances we can appreciate unprecedented fractional topological charge. As a consequence, using the expression reported in Eq. (5.15), it is also possible to compute the light's orbital angular momentum evolution along the propagation direction that is in turn fractional. In Fig. 5.6 it is reported the results of the computation of the OAM as a function of z .

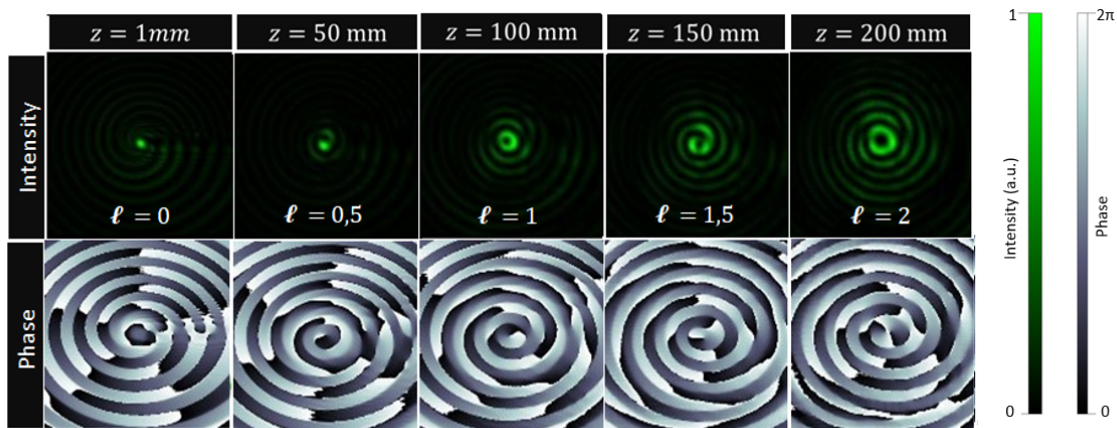


Figure 5.5: Simulated intensity (top row) and phase (bottom row) of the beam evolving its topological that charges linearly from $\ell = 0$ to $\ell = 2$. Phase and intensity profiles obtained at propagation distances: $z = 0$ cm, $z = 5$ cm, $z = 10$ cm, $z = 15$ cm, and $z = 20$ cm.

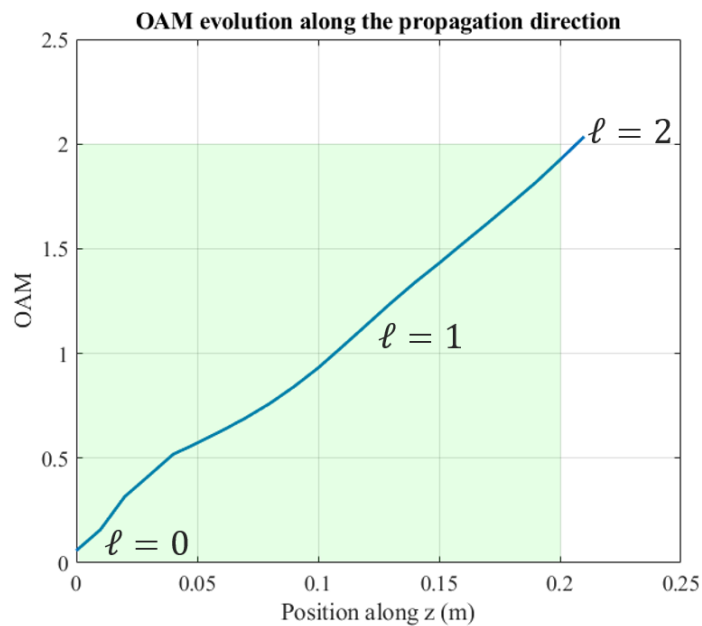


Figure 5.6: OAM evolution along the propagation direction. Linear transition. Result of the simulation.

5.4.2. Parabolic evolution of OAM

In order to obtain a parabolic variation of the topological charge along the propagation direction the expression of the morphological function $F_\ell(z)$ is the following:

$$F_\ell(z) = e^{i200\Phi z^2} \quad (5.20)$$

It follows that the expression of A_m computed from Eq. (5.16) is given by:

$$A_m = \sqrt{\pi} e^{-\frac{im^2\pi^2}{25\phi}} \operatorname{erf} \frac{15\phi - \pi m}{5\sqrt{i\phi}} i + \frac{\operatorname{erf} \frac{\pi m}{5\sqrt{i\phi}}}{105\sqrt{i\phi}} \quad (5.21)$$

The coefficient 200 in the exponential in Eq. (5.30) it is needed in order to obtain a topological charge $\ell = 1$ at 10cm and a topological charge $\ell = 4$ at distance of 20cm. The evaluation of Eq. (5.21) is not straightforward since the *erf* error function is defined only for real numbers while in this case its argument is complex. It was so necessary to introduce an approximation that is able to provides an excellent high-accuracy coverage over the required domain that has an extremely large computational cost. To better visualize the characteristics of this evolution we decreases the value of Q to $0.9995\frac{2\pi}{\lambda}$ so that it was possible to increase the number of Bessel beams that constitute the Frozen wave up to 93 ($2N+1$ with $N=46$). The results of the simulation are shown in Fig. 5.7. In Fig. 5.7 the evolution of the OAM along the propagation direction computed from Eq. (5.15) is reported.

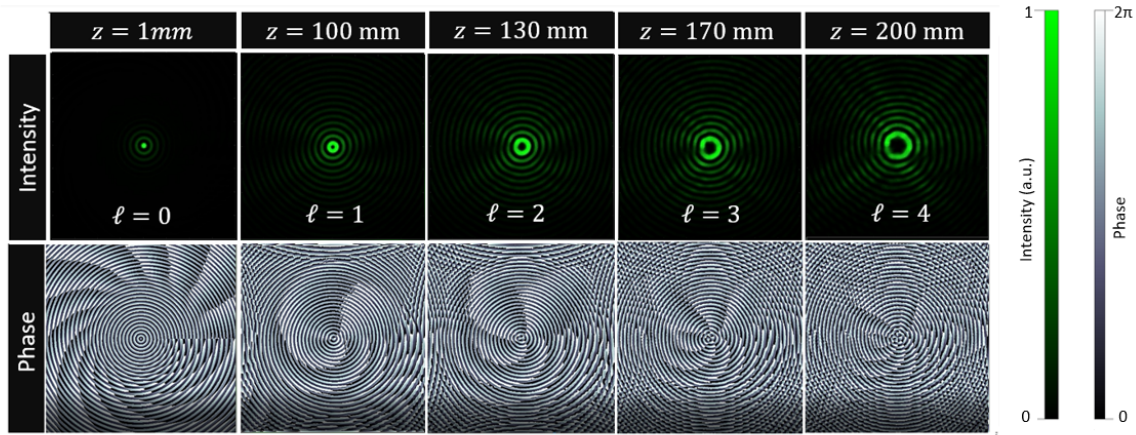


Figure 5.7: Simulated intensity (top row) and phase (bottom row) of the beam evolving its topological charge parabolically from $\ell = 0$ to $\ell = 4$. Phase and intensity profiles obtained at propagation distances: $z = 0$ cm, $z = 10$ cm, $z = 13$ cm, $z = 17$ cm, and $z = 20$ cm.

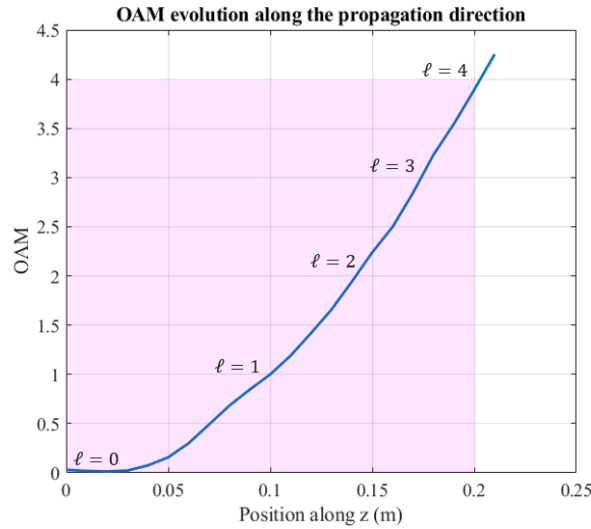


Figure 5.8: OAM evolution along the propagation direction. Parabolic evolution. Result of the simulation.

5.4.3. Experimental measurements

The experimental setup used to experimentally verify the simulation results is similar to the one shown in Fig. 5.9. The frozen wave were generated using programmable amplitude spatial lights modulator (SLM) where a computer-generated hologram (CGH) is mapped. Differently from the setup shown in figure, our SLM works in reflection mode.

A Gaussian beam was expanded, collimated, and imaged onto the SLM. The emerging beam is spatially filtered using a 4f system incorporating an iris to remove unwanted diffraction orders letting only the first order be able to go through. A CCD camera was then used to monitor the transverse intensity profile of the resulting beam with propagation. To collect different intensity patterns at different distances from the last lens of the 4f, the CCD is mounted on top of a moving stage that can control the position of the CCD camera. From the intensity patterns collected at different distances it was possible, using a modified and optimized version of the GS-algorithm to retrieve the phase of the field at each position[60].

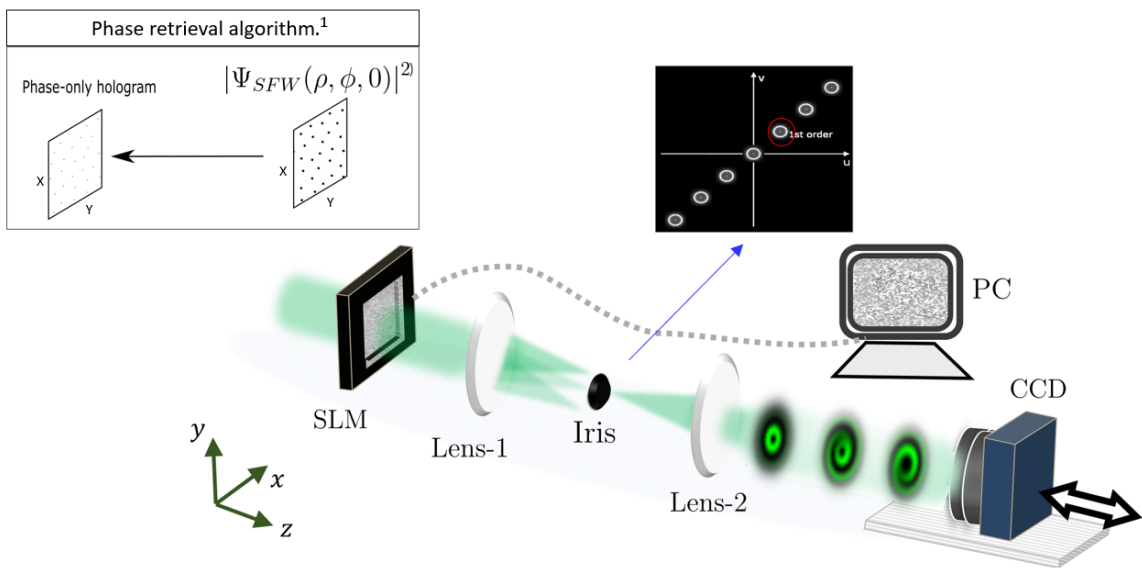


Figure 5.9: Experimental setup used to verify the simulation results. Figure from [58]

The results of the experimental measurements (both measured intensity and retrieved phase) are shown in Fig. 5.10 and Fig. 5.11 that are related respectively to step-like case and to the linear case. The parabolic evolution has not been measured yet. In Fig. 5.12 it is also possible to see how the OAM calculated from Eq. (5.15) using the data obtained from the experiments: the plots of the calculated OAM from the experimental data are consistent with the simulation results.

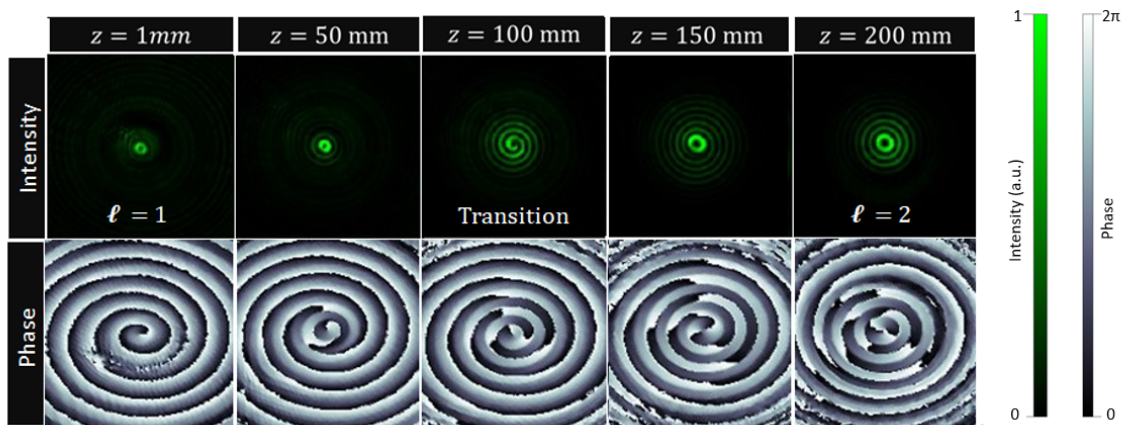


Figure 5.10: Measured intensity (top row) and retrieved phase (bottom row) of the beam evolving its topological charge from $\ell = 1$ to $\ell = 2$ with a step-like transition. Phase and intensity profiles obtained at propagation distances: $z = 0\text{ cm}$, $z = 5\text{ cm}$, $z = 10\text{ cm}$, $z = 15\text{ cm}$, and $z = 20\text{ cm}$.

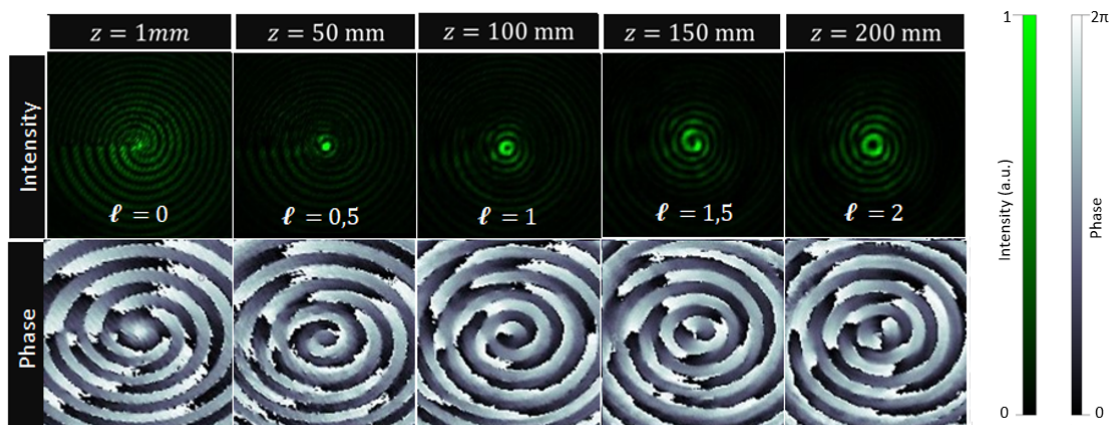
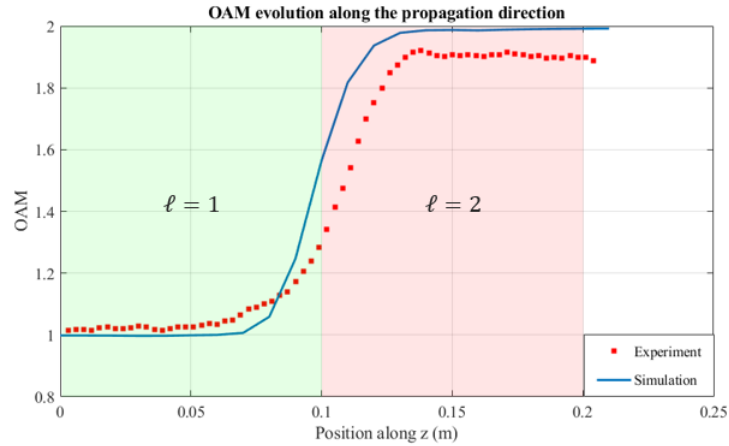
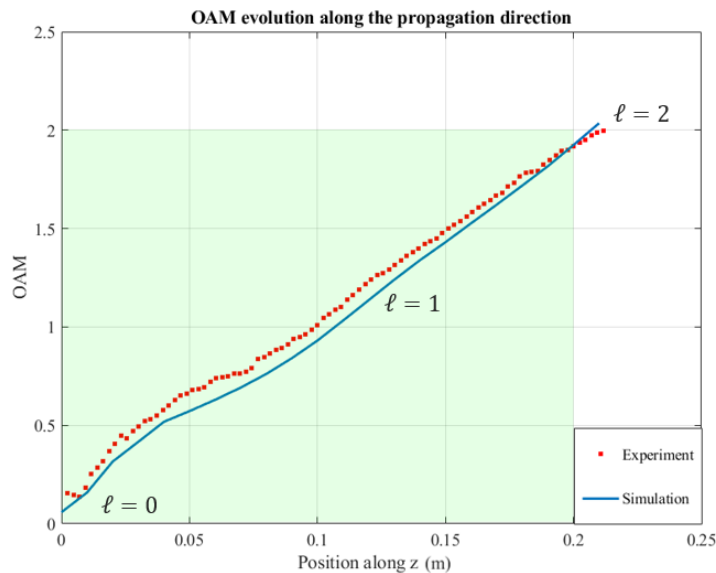


Figure 5.11: Measured intensity (top row) and retrieved phase (bottom row) of the beam evolving its topological charge linearly from $\ell = 0$ to $\ell = 2$. Phase and intensity profiles obtained at propagation distances: $z = 0\text{ cm}$, $z = 5\text{ cm}$, $z = 10\text{ cm}$, $z = 15\text{ cm}$, and $z = 20\text{ cm}$.



(a)



(b)

Figure 5.12: OAM evolution along the propagation direction computed from the data obtained from the experiment: **Top panel** : Step-like transition **Bottom panel** : Linear evolution.

5.5. Direct observation of spatially evolving Berry phase

In this section we show that, thanks to the method previously described, it is possible to observe that the orbital angular momentum evolution is accompanied by the accumulation

of a phase shift that is nothing else than the Berry phase [44]. Recalling that the expression of Frozen waves is given by Eq. (5.1) that define a FW as composed of $2N+1$ Bessel beams which are equally separated in the $k_{z,n}$ and centered at the longitudinal wavevector component $k_{z,0}$, it can be noticed that the superposition of Bessel beams acquires a propagation phase of $\sim e^{ik_{z,0}z}$. The variation of OAM that is introduced in the complex coefficient of the frozen waves contains a phase factor (as expressed in Eq. (5.15)) that if added to the dynamical phase, can be rewritten as

$$\sim e^{i(k_{z,0}z+\Phi(z))} \quad (5.22)$$

This additional phase factor can be related to the topological phase factor that is acquired whenever system undergoes a cyclic evolution governed by slow change in its parameter space, in this case, its orbital angular momentum and so it is nothing else than the geometric Berry phase Φ_{PB} . The variation of the phase $\Phi_{PB}(z)$ due to the varying orbital angular momentum implies that it is possible to define an additional wavevector component k_{PB} as $\frac{\partial\Phi_{PB}}{\partial z}$ that denotes a perturbation of the original value of $k_{z,0}$. From Eq. (5.2) it follows that also the transversal component needs to be modified accordingly to the variation of $k_{z,0}$. This shift manifests as a change in the beam's diameter. In order to confirm these statements we tested two different cases where it was possible to evaluate this acquired Berry-phase factor in the change of the size of the beam. We defined two sets of Frozen waves that linearly change their orbital angular momentum: in the first case the orbital angular momentum increase linearly from $\ell = 0$ to $\ell = 2$ in the interval between 0 and 10 cm and then linearly decreases from $\ell = 2$ to $\ell = 0$ in the range between 10cm and 20cm. In the second case the orbital angular momentum initially decreases linearly from $\ell = 2$ to $\ell = 0$ in the interval between 0 and 10cm and in the interval between 10cm and 20cm it linearly increase from $\ell = 2$ to $\ell = 0$. In the case of linearly increase-decrease variation of the orbital angular momentum (simulated results shown in Fig. 5.13 and experimental results shown in Fig. 5.14) it is possible to notice that the size of the beam depending on the slope of the transition (if it is increasing or decreasing). As an example, when the orbital angular momentum is $\ell = 1$ the size of the beam in the intensity patterns is different when the topological charge is increasing with respect to the case when it is decreasing; the diameter size at 5cm is in fact slightly larger with the respect to the diameter at 15cm. The effect is reversed in the case of the decreasing-increasing linear variation(simulated results shown in Fig. 5.15 and experimental results shown in Fig. 5.16) where the diameter at 15cm is larger with respect to the one at 5cm even if the topological charge in both cases is $\ell = 1$. The comparison between the OAM calculated from the simulation data and from the experimental data

are shown in Fig. 5.17.

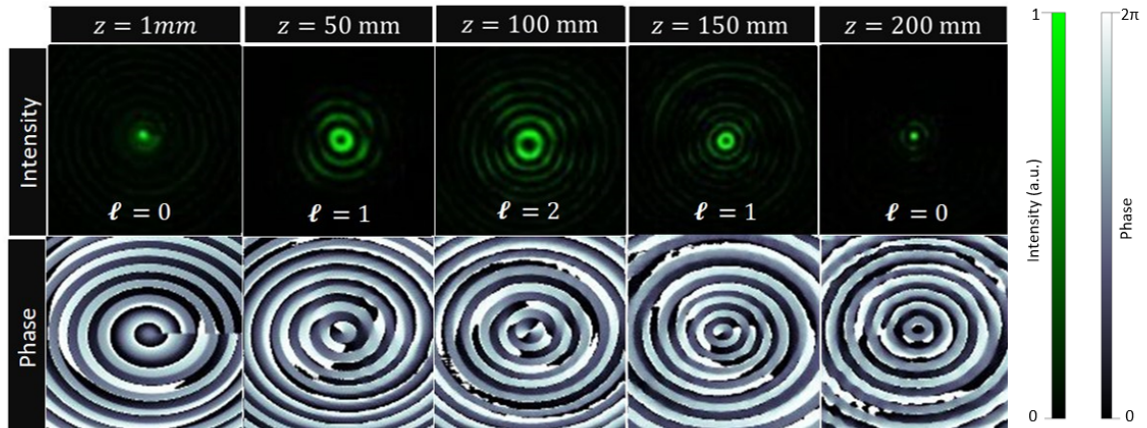


Figure 5.13: Simulated intensity (top row) and phase (bottom row) of the beam linearly increasing its topological charge from $\ell = 0$ to $\ell = 2$ and then linearly decreasing from $\ell = 2$ to $\ell = 0$. Phase and intensity profiles obtained at propagation distances: $z = 0\text{ cm}$, $z = 5\text{ cm}$, $z = 10\text{ cm}$, $z = 15\text{ cm}$, and $z = 20\text{ cm}$.

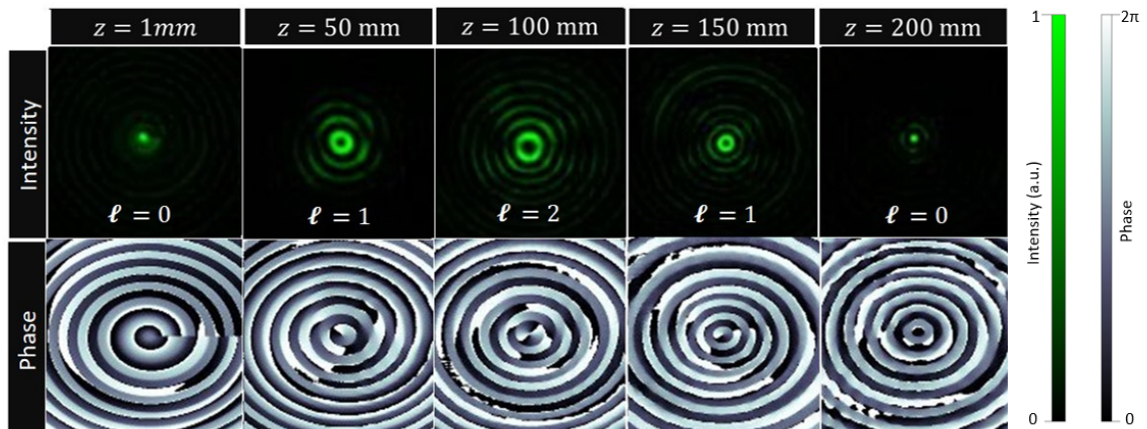


Figure 5.14: Measured intensity (top row) and retrieved phase (bottom row) of the beam linearly increasing its topological charge from $\ell = 0$ to $\ell = 2$ and then linearly decreasing from $\ell = 2$ to $\ell = 0$. Phase and intensity profiles obtained at propagation distances: $z = 0\text{ cm}$, $z = 5\text{ cm}$, $z = 10\text{ cm}$, $z = 15\text{ cm}$, and $z = 20\text{ cm}$.

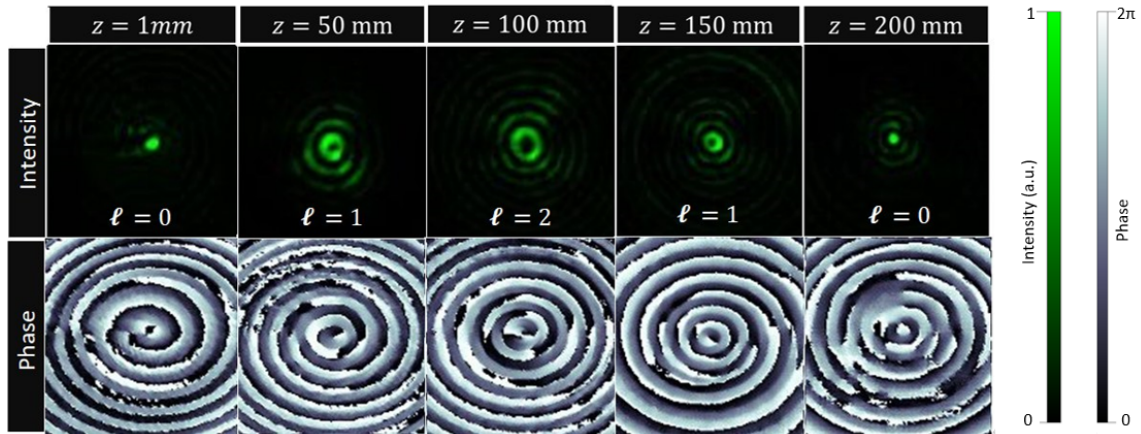


Figure 5.15: Simulated intensity (top row) and phase (bottom row) of the beam linearly decreasing its topological charge from $\ell = 2$ to $\ell = 0$ and then linearly increasing from $\ell = 0$ to $\ell = 2$. Phase and intensity profiles obtained at propagation distances: $z = 0\text{ cm}$, $z = 5\text{ cm}$, $z = 10\text{ cm}$, $z = 15\text{ cm}$, and $z = 20\text{ cm}$.

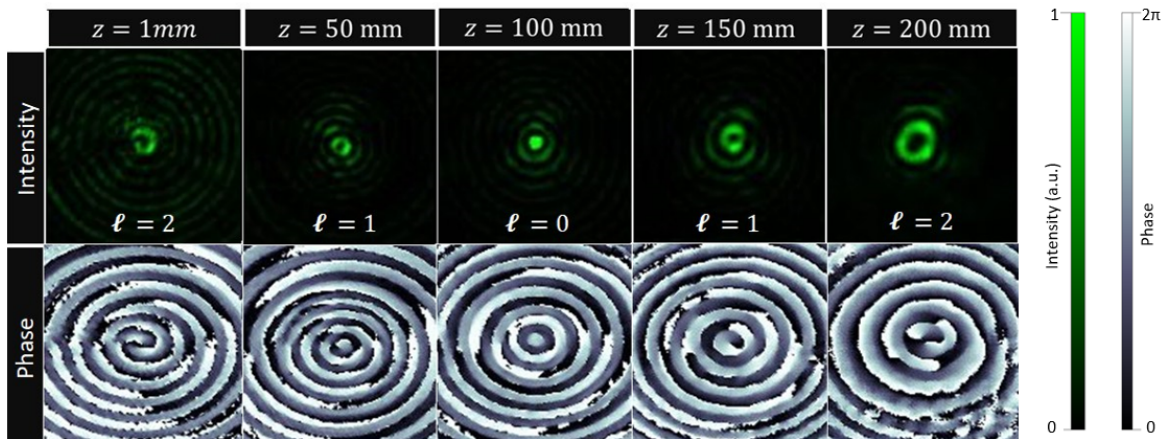
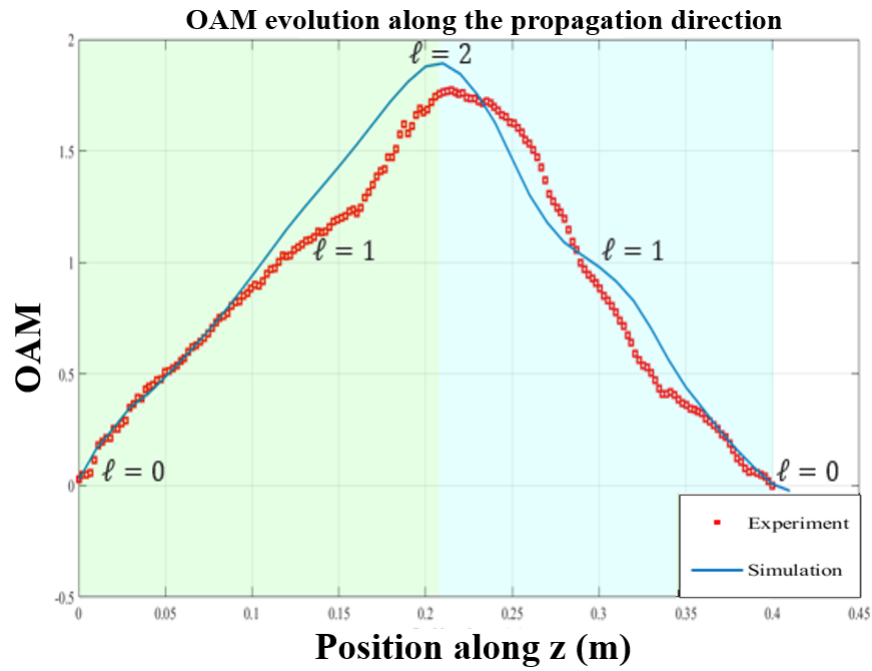
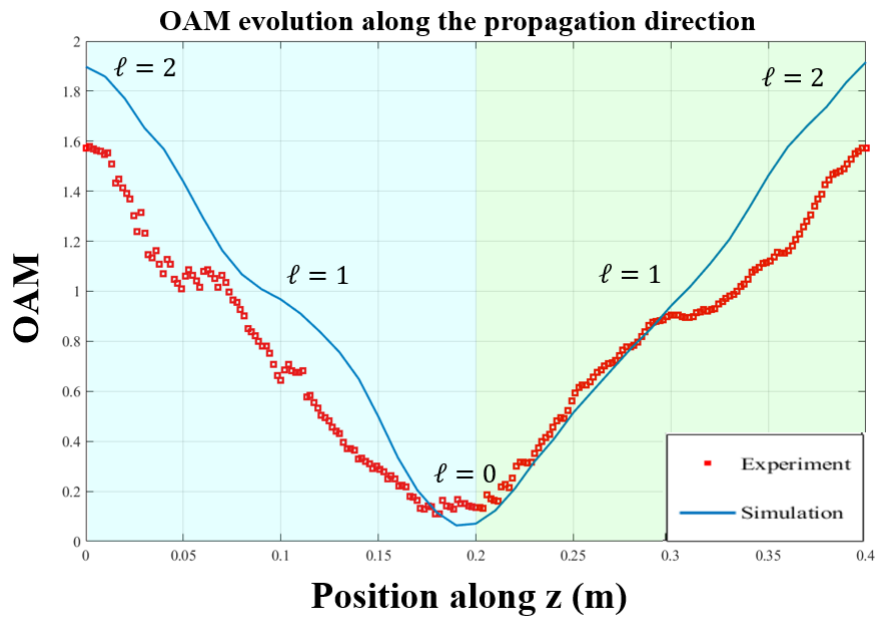


Figure 5.16: Measured intensity (top row) and retrieved phase (bottom row) of the beam linearly decreasing its topological charge from $\ell = 2$ to $\ell = 0$ and then linearly increasing from $\ell = 0$ to $\ell = 2$. Phase and intensity profiles obtained at propagation distances: $z = 0\text{ cm}$, $z = 5\text{ cm}$, $z = 10\text{ cm}$, $z = 15\text{ cm}$, and $z = 20\text{ cm}$.



(a)



(b)

Figure 5.17: OAM evolution along the propagation direction with Berry phase accumulation: **Top panel** : Linear increase of the topological charge from $\ell = 0$ to $\ell = 2$ followed by a linear decrease from $\ell = 2$ to $\ell = 0$. **Bottom panel** : Linear decrease of the topological charge from $\ell = 2$ to $\ell = 0$ followed by a linear increase from $\ell = 0$ to $\ell = 2$.

6 | Conclusions and future developments

In this work, we studied two emerging wavefront shaping tools, metasurfaces and spatial light modulators, and investigated their use in generating new classes of structured light. We proposed and demonstrated a strategy to design a bilayer metasurface and have shown a possible application. Starting from a library of a single layer metasurface, it was demonstrated that it is possible to assume that the two fins composing the bilayer metasurface can be considered as decoupled independently on the relative rotation between the two fins and on the fin geometries both in transmission and reflection mode. These results enable to overcome some of the limitations of a single layer metasurface enabling new possibilities in the wavefront shaping. As an example, a geometric metasurface has been designed: depending on the relative rotation between the two nanofins a different Berry phase is accumulated along the optical path. Some generalization of the proposed device working also on elliptical polarization can be developed in the future. In the context of structured light, the concept of Berry phase has been discussed also in association with optical vortices. Starting from Frozen waves formalism a new method to obtain a continuous variation of the OAM along the propagation direction has been developed and experimentally demonstrated. This method allows to tune at will the spatial derivative of the momentum (named "torque" in association with the temporal derivative of the momentum) and also the second order derivative, for the first time observed, named "Rotatum". These new degrees of freedom in beam manipulation can be utilized in many applications such as optical trapping, dense data communications, and remote sensing and imaging, leading to further advances in the context of structured light. With recent advances in wavefront shaping, new classes of structured light will keep emerging. The key is the achievement of a dynamical control of all degrees of freedom of light with high spatial and temporal resolution in space and time. With this versatile level of control, this rapidly growing area will help unlock new optical phenomena in the next years, ranging from the atomic to the astrophysical scale.

Bibliography

- [1] Ahmed H. Dorrah and Federico Capasso. Tunable structured light with flat optics. *Science*, 376(6591):eabi6860, 2022.
- [2] R. Clark Jones. A new calculus for the treatment of optical systemsi. description and discussion of the calculus. *J. Opt. Soc. Am.*, 31(7):488–493, Jul 1941.
- [3] Henry Hurwitz and R. Clark Jones. A new calculus for the treatment of optical systemsii. proof of three general equivalence theorems. *J. Opt. Soc. Am.*, 31(7):493–499, Jul 1941.
- [4] R. Clark Jones. A new calculus for the treatment of optical systemsiii. the sohncke theory of optical activity. *J. Opt. Soc. Am.*, 31(7):500–503, Jul 1941.
- [5] R. Clark Jones. A new calculus for the treatment of optical systems. iv. *J. Opt. Soc. Am.*, 32(8):486–493, Aug 1942.
- [6] J. B. Pendry. Negative refraction makes a perfect lens. *Phys. Rev. Lett.*, 85:3966–3969, Oct 2000.
- [7] Michaël Lobet, Iñigo Liberal, Larissa Vertchenko, Andrei V. Lavrinenko, Nader Engheta, and Eric Mazur. Momentum considerations inside near-zero index materials. *Light: Science & Applications*, 11(1):110, Apr 2022.
- [8] Guixin Li, Alexandra Boltasseva, and Said Zouhdi. Feature issue introduction: Metamaterials, photonic crystals and plasmonics. *Opt. Mater. Express*, 9(5):2400–2405, May 2019.
- [9] R.W. Wood. Xlii. on a remarkable case of uneven distribution of light in a diffraction grating spectrum. *The London, Edinburgh, and Dublin Philosophical Magazine and Journal of Science*, 4(21):396–402, 1902.
- [10] Nanfang Yu, Patrice Genevet, Mikhail A. Kats, Francesco Aieta, Jean-Philippe Tetienne, Federico Capasso, and Zeno Gaburro. Light propagation with phase discontinuities: Generalized laws of reflection and refraction. *Science*, 334(6054):333–337, 2011.

- [11] Ebrahim Karimi, Sebastian A. Schulz, Israel De Leon, Hammam Qassim, Jeremy Upham, and Robert W. Boyd. Generating optical orbital angular momentum at visible wavelengths using a plasmonic metasurface. *Light: Science & Applications*, 3(5):e167–e167, May 2014.
- [12] Francesco Aieta, Patrice Genevet, Mikhail Kats, and Federico Capasso. Aberrations of flat lenses and aplanatic metasurfaces. *Opt. Express*, 21(25):31530–31539, Dec 2013.
- [13] Lingling Huang, Xianzhong Chen, Holger Mühlenbernd, Hao Zhang, Shumei Chen, Benfeng Bai, Qiaofeng Tan, Guofan Jin, Kok-Wai Cheah, Cheng-Wei Qiu, Jensen Li, Thomas Zentgraf, and Shuang Zhang. Three-dimensional optical holography using a plasmonic metasurface. *Nature Communications*, 4(1):2808, Nov 2013.
- [14] Ronold W. P. King. *The Theory of Linear Antennas*. Harvard University Press, Cambridge, MA and London, England, 2013.
- [15] Mikhail A. Kats, Nanfang Yu, Patrice Genevet, Zeno Gaburro, and Federico Capasso. Effect of radiation damping on the spectral response of plasmonic components. *Opt. Express*, 19(22):21748–21753, Oct 2011.
- [16] Seyedeh Mahsa Kamali, Ehsan Arbabi, Amir Arbabi, and Andrei Faraon. A review of dielectric optical metasurfaces for wavefront control. *Nanophotonics*, 7(6):1041–1068, 2018.
- [17] Michael Faraday. The bakerian lecture: Experimental relations of gold (and other metals) to light. *Philosophical Transactions of the Royal Society of London*, 147:145–181, 1857.
- [18] Gustav Mie. Beiträge zur optik trüber medien, speziell kolloidaler metallösungen. *Annalen der Physik*, 330(3):377–445, 1908.
- [19] Manuel Decker, Isabelle Staude, Matthias Falkner, Jason Dominguez, Dragomir N. Neshev, Igal Brener, Thomas Pertsch, and Yuri S. Kivshar. High-efficiency dielectric huygens’ surfaces. *Advanced Optical Materials*, 3(6):813–820, 2015.
- [20] Shane Colburn, Alan Zhan, Elyas Bayati, James Whitehead, Albert Ryou, Luocheng Huang, and Arka Majumdar. Broadband transparent and cmos-compatible flat optics with silicon nitride metasurfaces

invited

. *Opt. Mater. Express*, 8(8):2330–2344, Aug 2018.

- [21] David Sell, Jianji Yang, Sage Doshay, Kai Zhang, and Jonathan A. Fan. Visible light metasurfaces based on single-crystal silicon. *ACS Photonics*, 3(10):1919–1925, Oct 2016.
- [22] Robert C. Devlin, Mohammadreza Khorasaninejad, Wei Ting Chen, Jaewon Oh, and Federico Capasso. Broadband high-efficiency dielectric metasurfaces for the visible spectrum. *Proceedings of the National Academy of Sciences*, 113(38):10473–10478, 2016.
- [23] Noah A. Rubin, Zhujun Shi, and Federico Capasso. Polarization in diffractive optics and metasurfaces. *Adv. Opt. Photon.*, 13(4):836–970, Dec 2021.
- [24] Ehsan Arbabi, Seyedeh Mahsa Kamali, Amir Arbabi, and Andrei Faraon. Full-stokes imaging polarimetry using dielectric metasurfaces. *ACS Photonics*, 5(8):3132–3140, Aug 2018.
- [25] Noah A. Rubin, Gabriele D’Aversa, Paul Chevalier, Zhujun Shi, Wei Ting Chen, and Federico Capasso. Matrix fourier optics enables a compact full-stokes polarization camera. *Science*, 365(6448):eaax1839, 2019.
- [26] M. Khorasaninejad, A. Y. Zhu, C. Roques-Carmes, W. T. Chen, J. Oh, I. Mishra, R. C. Devlin, and F. Capasso. Polarization-insensitive metalenses at visible wavelengths. *Nano Letters*, 16(11):7229–7234, Nov 2016.
- [27] J. P. Balthasar Mueller, Noah A. Rubin, Robert C. Devlin, Benedikt Groever, and Federico Capasso. Metasurface polarization optics: Independent phase control of arbitrary orthogonal states of polarization. *Phys. Rev. Lett.*, 118:113901, Mar 2017.
- [28] Amir Arbabi, Yu Horie, Mahmood Bagheri, and Andrei Faraon. Dielectric metasurfaces for complete control of phase and polarization with subwavelength spatial resolution and high transmission. *Nature Nanotechnology*, 10(11):937–943, Nov 2015.
- [29] Anders Pors, Ole Albrektsen, Ilya P. Radko, and Sergey I. Bozhevolnyi. Gap plasmon-based metasurfaces for total control of reflected light. *Scientific Reports*, 3(1):2155, Jul 2013.
- [30] Fei Cheng, Lei Ding, Liangyu Qiu, Daniel Nikolov, Aaron Bauer, Jannick P. Rolland, and A. Nick Vamivakas. Polarization-switchable holograms based on efficient, broadband multifunctional metasurfaces in the visible regime. *Opt. Express*, 26(23):30678–30688, Nov 2018.
- [31] Yuanmu Yang, Wenyi Wang, Parikshit Moitra, Ivan I. Kravchenko, Dayrl P. Briggs,

- and Jason Valentine. Dielectric meta-reflectarray for broadband linear polarization conversion and optical vortex generation. *Nano Letters*, 14(3):1394–1399, Mar 2014.
- [32] Eliahu Cohen, Hugo Larocque, Frédéric Bouchard, Farshad Nejdassattari, Yuval Gefen, and Ebrahim Karimi. Geometric phase from aharonov–bohm to pancharatnam–berry and beyond. *Nature Reviews Physics*, 1(7):437–449, Jul 2019.
- [33] Berry M. *Quantal phase factors accompanying adiabatic changes*. Proc. R. Soc., 1984.
- [34] S. Pancharatnam. Generalized theory of interference, and its applications. *Proceedings of the Indian Academy of Sciences - Section A*, 44:247–262, 1956.
- [35] Biener G. Space-variant pancharatnam–berry phase optical elements with computer-generated subwavelength gratings. *OPTICS LETTER*, (13), 2002.
- [36] You Zhou, Ivan I. Kravchenko, Hao Wang, Hanyu Zheng, Gong Gu, and Jason Valentine. Multifunctional metaoptics based on bilayer metasurfaces. *Light: Science & Applications*, 8(1):80, Sep 2019.
- [37] Katsuya Tanaka, Dennis Arslan, Stefan Fasold, Michael Steinert, Jürgen Sautter, Matthias Falkner, Thomas Pertsch, Manuel Decker, and Isabelle Staude. Chiral bilayer all-dielectric metasurfaces. *ACS Nano*, 14(11):15926–15935, Nov 2020.
- [38] Juan Deng, Fan Gao, Peicheng Yuan, Yun Li, and Bo Yan. Bidirectional nanoprinting based on bilayer metasurfaces. *Opt. Express*, 30(1):377–388, Jan 2022.
- [39] Rzeszotnik Z. A note on factoring unitary matrices. *ScienceDirect*, 2018.
- [40] Simon R. Evolving geometric phase and its dynamical manifestation as a frequency shift: An optical experiment. *PHYSICAL REVIEW LETTERS*, 1988.
- [41] Dennis R. Pape and Larry J. Hornbeck. Characteristics Of The Deformable Mirror Device For Optical Information Processing. *Optical Engineering*, 22(6):226675, 1983.
- [42] David L. Flannery, Anne Marie Biernacki, John S. Loomis, and Steven L. Cartwright. Real-time coherent correlator using binary magneto optic spatial light modulators at input and fourier planes. *Appl. Opt.*, 25(4):466–466, Feb 1986.
- [43] Jullien, Aurélie. Spatial light modulators. *Photoniques*, (101):59–64, 2020.
- [44] Ahmed H. Dorrah, Noah A. Rubin, Aun Zaidi, Michele Tamagnone, and Federico Capasso. Metasurface optics for on-demand polarization transformations along the optical path. *Nature Photonics*, 15(4):287–296, Apr 2021.

- [45] J. Durnin, J. J. Miceli, and J. H. Eberly. Diffraction-free beams. *Phys. Rev. Lett.*, 58:1499–1501, Apr 1987.
- [46] Michel Zamboni-Rached. Stationary optical wave fields with arbitrary longitudinal shape by superposing equal frequency bessel beams: Frozen waves. *Opt. Express*, 12(17):4001–4006, Aug 2004.
- [47] Tárício A. Vieira, Michel Zamboni-Rached, and Marcos R.R. Gesualdi. Modeling the spatial shape of nondiffracting beams: Experimental generation of frozen waves via holographic method. *Optics Communications*, 315:374–380, 2014.
- [48] M. Zamboni-Rached and Mo Mojahedi. Shaping finite-energy diffraction- and attenuation-resistant beams through bessel-gauss-beam superposition. *Phys. Rev. A*, 92:043839, Oct 2015.
- [49] Tárício A. Vieira, Marcos R. R. Gesualdi, Michel Zamboni-Rached, and Erasmo Recami. Production of dynamic frozen waves: controlling shape, location (and speed) of diffraction-resistant beams. *Opt. Lett.*, 40(24):5834–5837, Dec 2015.
- [50] Ahmed H. Dorrah, Michel Zamboni-Rached, and Mo Mojahedi. Controlling the topological charge of twisted light beams with propagation. *Phys. Rev. A*, 93:063864, Jun 2016.
- [51] L. Allen, M. W. Beijersbergen, R. J. C. Spreeuw, and J. P. Woerdman. Orbital angular momentum of light and the transformation of laguerre-gaussian laser modes. *Phys. Rev. A*, 45:8185–8189, Jun 1992.
- [52] M.J. Padgett and L. Allen. The poynting vector in laguerre-gaussian laser modes. *Optics Communications*, 121(1):36–40, 1995.
- [53] Alison M. Yao and Miles J. Padgett. Orbital angular momentum: origins, behavior and applications. *Adv. Opt. Photon.*, 3(2):161–204, Jun 2011.
- [54] S. S. R. Oemrawsingh, J. A. W. van Houwelingen, E. R. Eliel, J. P. Woerdman, E. J. K. Verstegen, J. G. Kloosterboer, and G. W. 't Hooft. Production and characterization of spiral phase plates for optical wavelengths. *Appl. Opt.*, 43(3):688–694, Jan 2004.
- [55] S. S. R. Oemrawsingh, J. A. W. van Houwelingen, E. R. Eliel, J. P. Woerdman, E. J. K. Verstegen, J. G. Kloosterboer, and G. W. 't Hooft. Production and characterization of spiral phase plates for optical wavelengths. *Appl. Opt.*, 43(3):688–694, Jan 2004.

- [56] Jani Tervo and Jari Turunen. Rotating scale-invariant electromagnetic fields. *Opt. Express*, 9(1):9–15, Jul 2001.
- [57] Christian Schulze, Filippus S. Roux, Angela Dudley, Ronald Rop, Michael Duparré, and Andrew Forbes. Accelerated rotation with orbital angular momentum modes. *Phys. Rev. A*, 91:043821, Apr 2015.
- [58] Ahmed H. Dorrah, Carmelo Rosales-Guzmán, Andrew Forbes, and Mo Mojahedi. Evolution of orbital angular momentum in three-dimensional structured light. *Phys. Rev. A*, 98:043846, Oct 2018.
- [59] Laura Rego, Kevin M. Dorney, Nathan J. Brooks, Quynh L. Nguyen, Chen-Ting Liao, Julio San Román, David E. Couch, Allison Liu, Emilio Pisanty, Maciej Lewenstein, Luis Plaja, Henry C. Kapteyn, Margaret M. Murnane, and Carlos Hernández-García. Generation of extreme-ultraviolet beams with time-varying orbital angular momentum. *Science*, 364(6447):eaaw9486, 2019.
- [60] Giancarlo Pedrini, Wolfgang Osten, and Yan Zhang. Wave-front reconstruction from a sequence of interferograms recorded at different planes. *Opt. Lett.*, 30(8):833–835, Apr 2005.
- [61] Percival Almoró, Giancarlo Pedrini, and Wolfgang Osten. Complete wavefront reconstruction using sequential intensity measurements of a volume speckle field. *Appl. Opt.*, 45(34):8596–8605, Dec 2006.

A | Appendix A - Bilayer simulation: the effect of a relative rotation of 45° sweeping the dimensions of the top nanofin fixing the dimension of the bottom nanofin

In chapter 3 we analyzed the effect of a relative rotation when both the bottom and top nanofin dimensions were fixed. On the other hand it is not guaranteed that the relative rotation does not significantly effect the assumption of decoupling between the two nanofins. In order to verify if the assumption of decoupling is valid also when a relative rotation between the nanofins constituting the metasurface we simulated a bilayer structure with the bottom nanofin dimensions fixed, sweeping the dimension of the top nanofin that is rotated with respect to the bottom one by an angle of 45° . The dimension of the bottom nanofin are the one of the QWP_1 ($134\text{nm} \times 202\text{nm}$). This was useful to identify the geometries for which the error between the analytical and the simulated Jones matrix is maximum. In the following figures the errors of the diagonal elements of the Jones matrix (phase in Fig. A.1) and amplitude in Fig. A.2)) are reported: as it can be noticed the error is very low for most of the simulated geometries. The error is maximum in correspondence of the geometries that have one dimension much bigger with the respect to the other one: in these cases a relevant portion of the top nanofin is exceeding the dimension of the basis of the bottom nanofin so reflections can happen between it and the substrate.

A| Appendix A - Bilayer simulation: the effect of a relative rotation of 45° sweeping the dimensions of the top nanofin fixing the dimension of the bottom nanofin

78

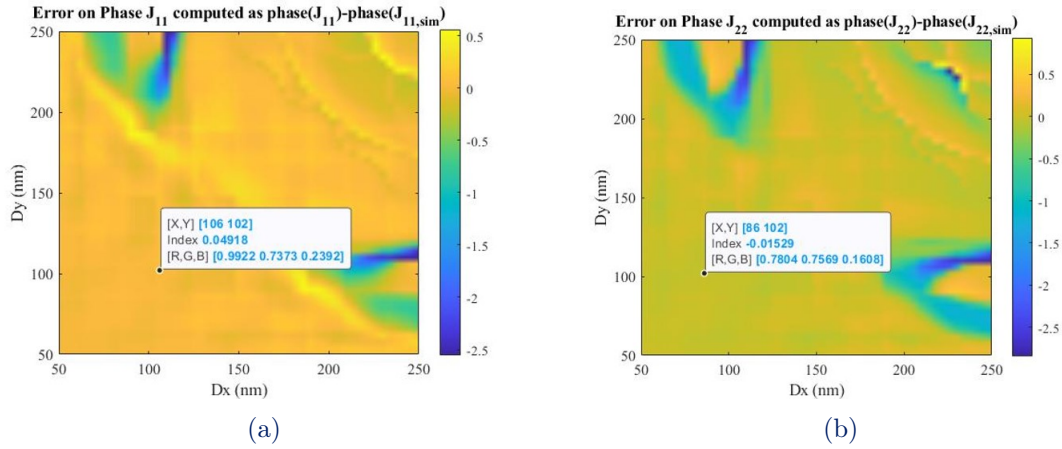


Figure A.1: Plots of the difference in magnitude between the Jones matrix elements of the simulated bilayer with bottom fin fixed and the Jones matrix elements of a bilayer analytically computed. Relative rotation between the nanofins: 45. **(a)** : Difference between the phase of J_{11} extracted from the simulation and the phase of J_{11} analytically computed from the data of the single layer. **(b)** : Difference between the phase of J_{22} extracted from the simulation and the phase of J_{22} analytically computed from the data of the single layer.

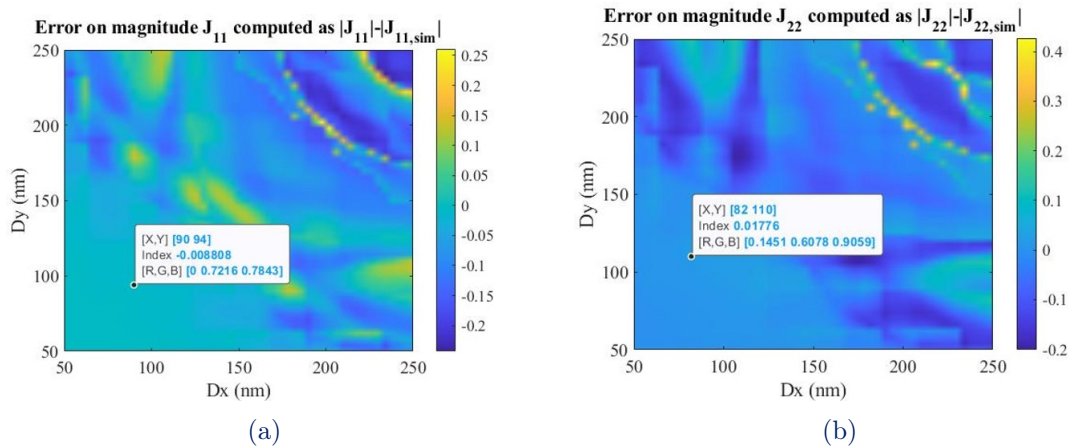


Figure A.2: Plots of the difference in magnitude between the Jones matrix elements of the simulated bilayer with bottom fin fixed and the Jones matrix elements of a bilayer analytically computed. Relative rotation between the nanofins: 45. **(a)** : Difference between the magnitude of J_{11} extracted from the simulation and the magnitude of J_{11} analytically computed from the data of the single layer. **(b)** : Difference between the magnitude of J_{22} extracted from the simulation and the magnitude of J_{22} analytically computed from the data of the single layer.

B | Phase retrieval algorithm

The phase of the optical field at each position was obtained by a modified version of the single-beam multiple-intensity reconstruction (SBMIR) method. The CCD camera do not provide the complex amplitude of a wave field since it is not sensitive to the phase of the field and so this information is lost during the recording processes. On the other hand it has been shown that, recording at least two intensity patterns of the object at different positions and by application of iterative algorithms it is possible to retrieve also the phase profile. The algorithm here used is similar to the one presented in [61]. The presented algorithm works as follows: $n + 1$ intensity patterns are recorded using a CCD camera at equidistant positions (Δz is the distance between two images); once all the patterns have been collected, a constant phase ($\phi_0 = 0$) is assumed for the intensity pattern at the origin ($z_0 = 0$) so that it is possible to write a wave front of the form $\sqrt{I_0}e^{i\phi_0}$ that is then propagated from $z_0 = 0$ to $z_1 = z_0 + \Delta z$ using the Rayleigh–Sommerfeld relation. The obtained complex amplitude given by $A_1e^{i\phi_1}$ is then rearranged as follows: the term $e^{i\phi_1}$ is combined with the square root of the measured intensity so that the new complex wave front at the position $z_1 = z_0 + \Delta z$ is given by $\sqrt{I_1}e^{i\phi_0}$ ready to be propagated to the new position $z_2 = z_0 + 2\Delta z$. The same procedure is so repeated for all the other intensity patterns until the last one at the position $z_n = z_0 + n\Delta z$. Once also this last complex amplitude has been obtained, the same process is repeated using back-propagation Rayleigh–Sommerfeld relation.

The modified version of the presented method is depicted in Fig. B.1. The distance between two different intensity patterns can vary from $\Delta z = 0.25mm$ up to $\Delta z = 1mm$ depending on the pattern and 300 images were collected in total. Differently from what has been described above, during each propagation step, we use the measured intensity profile and the retrieved phase profile as the initial boundary conditions for the propagation. The resultant forward or backward propagated field phase at the target plane then becomes the updated retrieved phase at the target plane. The starting retrieved phase estimated for all planes is random between 0 and 2π . Each cycle has been repeated 2000 times or if convergence has been reached: to reach convergence it was necessary that the root-mean-squared (RMS) deviation between the estimated intensity (each normalized by their

respective maximum intensities) after a propagation step and the true intensity map at that plane was lower than a certain threshold. Differently from the method presented above Fresnel and Fraunhofer diffraction formula were used to propagate the field from one position to another depending on the propagation distance. These modifications allowed to obtain better results with respect to the technique presented in [61].

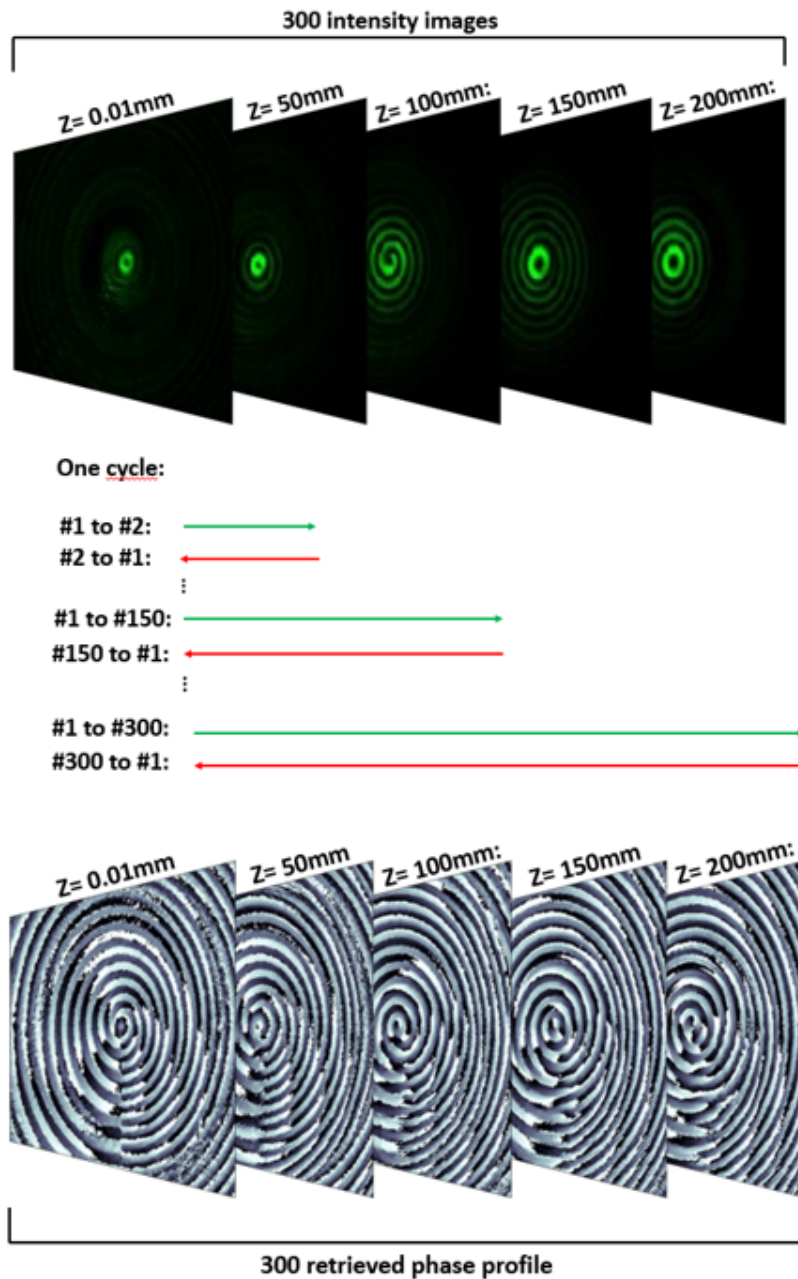


Figure B.1: Iterative single-beam multipleintensity reconstruction phase retrieval algorithm.

List of Figures

1.1	SEM image of plasmonic metasurface.	4
1.2	Model of dielectric metasurface.	7
2.1	Unit cell of the single layer metasurface.	10
2.2	Simulation results of a single layer metasurface.	11
2.3	Unit cell of the single layer metasurface. The nanofin is rotated around its geometrical center by an angle θ	11
2.4	Poincaré sphere.	14
2.5	Symmetry analysis of a single layer metasurface.	16
3.1	A schematic of the bilayer metasurface.	19
3.2	Unit cell of the bilayer metasurface.	21
3.3	Simulation results of a bilayer metasurface with the dimension of the bottom fin fixed.	25
3.4	Plots of the difference in magnitude between the Jones matrix elements of the simulated bilayer with bottom fin fixed and the Jones matrix elements of a bilayer analytically computed.	26
3.5	Plots of the difference in phase between the Jones matrix elements of the simulated bilayer with bottom fin fixed and the Jones matrix elements of a bilayer analytically computed.	26
3.6	Plots of the difference in phase between the Jones matrix elements of the simulated bilayer with bottom fin fixed and the Jones matrix elements of a bilayer analytically computed showing the ability of the bilayer metasurface to cover 0 to 2π phase range.	27
3.7	Plots of the analytical Jones matrix of a bilayer computed as the product of the Jones matrices of a single layer.	29
3.8	Plots of the simulated Jones matrix of a bilayer metasurface.	29
3.9	Plots of the error between the simulated Jones matrix of a bilayer metasurface and the analytical Jones Matrix computed as product of Jones matrix of a single layer.	30

3.10	Model of a bilayer metasurface in reflection. The silver layer represents the mirror. The yellow arrow represents the incident light.	31
3.11	Unit cell of a single layer metasurface working in reflection mode. The silver sheet represents a 150nm thick Aluminum mirror. The structure is illuminated from the top as denoted by the yellow arrow.	32
3.12	Comparison of the power transmission plots between a simulated single layer metasurface in reflection and the results obtained from the product of Jones matrix	33
3.13	Comparison of the phase shift plots between a simulated single layer metasurface in reflection and the results obtained from the product of Jones matrix	33
3.14	Unit cell of a single layer metasurface working in reflection mode with the addition of a silica spacer. The silver sheet represents a 150nm thick Aluminum mirror. The structure is illuminated from the top as denoted by the yellow arrow.	34
3.15	Comparison of the phase shift plots between a simulated single layer metasurface in reflection with the addition of an optimum spacer addition and the results obtained from the product of Jones matrix	35
3.16	Plots of the error between the simulated Jones matrix of a single layer metasurface in reflection and the analytical Jones Matrix computed as product of Jones matrix of a single layer in transmission.	36
3.17	Optimum spacer dimension as a function of the nanofin geometry.	36
3.18	Unit cell of a bilayer metasurface working in reflection mode with the addition of a silica spacer.	37
3.19	Plots of the difference in magnitude between the Jones matrix elements of the simulated bilayer in reflection with bottom fin fixed and the In analogy to the case of single layer metasurface Jones matrix elements of a bilayer analytically computed	38
3.20	Plots of the difference in phase between the Jones matrix elements of the simulated bilayer in reflection with bottom fin fixed and the analytically computed Jones Matrix elements of a bilayer	39
3.21	Experimental arrangement for the generation of a time-varying geometric phase. The basic configuration is that of a Michelson interferometer. Figure from [40]	40
3.22	Evolution of polarization on the Poincare sphere	41
3.23	Model of the designed grating.	42
3.24	Fraction of transmitted power as a function of diffracted angle	42

List of Figures	83
4.1 Liquid Crystal Spatial light modulator	46
4.2 Implementation of spatially varying polarization control with configurations of spatial light modulators (SLMs).	47
5.1 Longitudinal intensity function obtained with Frozen waves	51
5.2 Examples of helical phase fronts	52
5.3 Simulated intensity and phase of step-like transition of topological charge.	55
5.4 Calculated OAM. Step-like transition.	56
5.5 Simulated intensity and phase. Linear variation of topological charge.	58
5.6 OAM evolution along the propagation direction. Linear transition. Result of the simulation.	58
5.7 Simulated intensity and phase. Parabolic variation of topological charge.	60
5.8 OAM evolution along the propagation direction. Parabolic evolution. Result of the simulation.	60
5.9 Experimental setup used to verify the simulation results. Figure from [58]	61
5.10 Measured intensity and retrieved phase of the beam evolving its topological charge from $\ell = 1$ to $\ell = 2$ with a step-like transition.	62
5.11 Measured intensity and retrieved phase of the beam linearly evolving its topological charge from $\ell = 1$ to $\ell = 2$	62
5.12 OAM evolution along the propagation direction computed from the data obtained from the experiment.	63
5.13 Simulated intensity and phase of the beam linearly increasing its topological charge from $\ell = 0$ to $\ell = 2$ and then linearly decreasing from $\ell = 2$ to $\ell = 0$	65
5.14 Measured intensity and retrieved phase of the beam linearly increasing its topological charge from $\ell = 0$ to $\ell = 2$ and then linearly decreasing from $\ell = 2$ to $\ell = 0$	65
5.15 Simulated intensity and phase of the beam linearly decreasing its topological charge from $\ell = 2$ to $\ell = 0$ and then linearly increasing from $\ell = 0$ to $\ell = 2$	66
5.16 Measured intensity and retrieved phase of the beam linearly decreasing its topological charge from $\ell = 2$ to $\ell = 0$ and then linearly increasing from $\ell = 0$ to $\ell = 2$	66
5.17 OAM evolution along the propagation direction with Berry phase accumulation.	67

A.1	Plots of the difference in magnitude between the Jones matrix elements of the simulated bilayer with bottom fin fixed and the Jones matrix elements of a bilayer analytically computed. Relative rotation between the nanofins: 45	78
A.2	Plots of the difference in phase between the Jones matrix elements of the simulated bilayer with bottom fin fixed and the Jones matrix elements of a bilayer analytically computed. Relative rotation between the nanofins: 45.	78
B.1	Iterative single-beam multipleintensity reconstruction phase retrieval algorithm.	80

List of Tables

2.1	Jones matrix elements of two possible QWP	13
3.1	Element-by-element comparison between the magnitude of the Jones matrix elements of the simulated bilayer \mathbf{J}_s and the elements of the analytical Jones matrix \mathbf{J}_a for the QWP ₁ (134nm × 202nm)	22
3.2	Element-by-element comparison of the phase of the Jones matrix elements of the simulated bilayer \mathbf{J}_s and the elements of the analytical Jones matrix \mathbf{J}_a QWP ₁ (134nm × 202nm)	22
3.3	Element-by-element comparison of the magnitude of the Jones matrix elements of the simulated bilayer \mathbf{J}_s and the elements of the analytical Jones matrix \mathbf{J}_a for the QWP ₂ (114nm × 154nm)	23
3.4	Element-by-element comparison of the phase of the Jones matrix elements of the simulated bilayer \mathbf{J}_s and the elements of the analytical Jones matrix \mathbf{J}_a QWP ₂ (114nm × 154nm)	23

List of Symbols

Variable	Description
<i>QWP</i>	quarter wave plate
RCP	right circularly polarized
LCP	left circularly polarized
FW	frozen wave
LC	liquid crystal
SLM	spatial light modulator
CMOS	complementary metal-oxide semiconductor
RIE	reactive ion etching

Acknowledgements

At times, our own light goes out and is rekindled by a spark from another person. Each of us has cause to think with deep gratitude of those who have lighted the flame within us.

I am extremely thankful to my advisor Professor Federico Capasso of the School of Engineering and Applied Science at Harvard University: he gave me the opportunity to join his group and to approach a vibrant and exciting research field in the world of Photonics and Metamaterials: he perspires a passion for science that is able to fire the love for the research into everyone.

Part of the work presented in my thesis is in collaboration with Dr. Ahmed H. Dorrah to whom I acknowledge the paternity of the grating design with the metasurface bilayer and the concept of Rotatum.

It is almost difficult for me to thank Dr. Ahmed H. Dorrah as much as he deserves: not only did he follow me step by step in my research, not only did he have the patience to explain to me several times some concepts that were new to me but he was my most important point of reference at Harvard during these last months. For me he is and will always be not a simple colleague but the mentor that I have observed and listened to with meticulous attention every single day because I saw in him what I would like to be tomorrow, as a scholar and as a man.

I would especially like to thank my mum and my dad who have supported and put up with me since I was born. In their words I have always found the trust a child needs and everything I have achieved to date I owe almost exclusively to their love. They were the perfect parents and will always be a point of reference for me in life.

I would like to thank my grandfather Alfonso, a mathematics teacher who followed me as a child, and my grandfather Pietro, an engineer who unfortunately passed away when I was only 9 months old: I am sure that my passion for science comes from them.

I thank my roommates, Alfredo and Vincenzo, forced to live with me and with my absurd habits.

I thank my friends from high school Italo, Antonio, Saverio, Damiano and Antonio. I

thank my friends Davide, Matteo, Giacomo, Alessandro, Lorenzo and Filippo who transformed my 5 years in Turin making them perhaps the best of my life.

I also want to thank Giulio and Mario, friends since my first day at university and that were able to make me feel home.

A special thanks to Federico: despite the kilometers we have hoped for over the years, the conversations with him have been fundamental for my growth as a man. I am lucky to have such an outspoken and sincere friend who is always there in times of need.

Thanks to Elisabetta, my class colleague who with her sweetness was able to brighten my day at the Politecnico.

I am and will be infinitely grateful to my brother Alberto: fate meant that we met many years ago at the Normale di Pisa for a few days, we met by chance on the first day of the first year of university and we became colleagues, friends, roommates and infinite siblings. If I've come this far, I owe a lot to your friendship.

Finally thanks to Maria, my better half with whom I have shared every single emotion in the last 7 years. The love I feel for you has led me to find the determination and strength to achieve this result and I hope it leads us to a life of joy and smiles together. Thank you for being close to me despite my enormous flaws and I hope one day I can give you back all that you have been able to give me with your love. If you smile then I'm sure I will smile too.